



Investigation of Parent-Well Production Induced Stress Interference in Multilayer Unconventional Reservoirs

Yanli Pei¹ · Kamy Sepehrnoori¹

Received: 30 September 2020 / Accepted: 14 November 2021 / Published online: 8 January 2022
© The Author(s), under exclusive licence to Springer-Verlag GmbH Austria, part of Springer Nature 2021

Abstract

A 3D explicitly coupled geomechanics and multiphase compositional model is developed with an embedded discrete fracture model (EDFM) and finite element method (FEM) to simulate the spatiotemporal stress evolution in a multilayer unconventional reservoir with complex fracture geometry. Different scenarios with and without interlayer geomechanical heterogeneity are studied to provide rules of thumb for infill drilling under the impacts of reservoir permeability, fracture penetration, differential stress, and rock stiffness. With a five-layer reservoir model setup—two parent wells located in the middle layer and the top and bottom layers being potential targets, numerical results show that (a) higher reservoir permeability aggravates the stress reorientation and reduces the magnitude of minimum horizontal stress (S_{hmin}) in both the production and potential targets; (b) fracture penetration has negligible influence on the stress evolution in the top and middle layers but speeds up the stress reversal in the bottom layer; (c) larger differential stress retards the orientation change of maximum horizontal stress (S_{Hmax}) more significantly in the bottom layer than in the top layer; (d) increasing rock stiffness of the top and bottom layers accelerates the stress reversal in these layers while an opposite response is observed in the middle layer.

Highlights

- A novel 3D coupled geomechanics and multiphase compositional model is developed to investigate multilayer stress interference.
- The complex fracture geometry is characterized by an embedded discrete fracture model (EDFM), and solid deformation is captured by the finite element method (FEM).
- The mechanisms of stress reorientation or stress redistribution spreading towards the top and bottom potential pay zones of stacked formations are proposed.
- Different scenarios with and without interlayer geomechanical heterogeneity are investigated to provide rules of thumb for the multilayer infill operations.

Keywords Stress interference · Multilayer unconventional reservoir · Interlayer heterogeneity · Geomechanics · Infill drilling · Complex fracture geometry

List of Symbols

A	Area, ft ²	\mathbf{D}	Stiffness tensor, psi
\mathbf{b}	Body force, ft s ⁻²	\mathbf{k}	Permeability tensor, mD
\mathbf{B}	Strain–displacement matrix, ft ⁻¹	L	Length, ft
d	Average distance, ft	n_c	Number of components, dimensionless
		\mathbf{n}	Normal vector to a plane, dimensionless
		N_i	Number of moles of component i , mole
		N_p	Number of phases, dimensionless
		\mathbf{N}	Shape function vector, dimensionless
		P	Pressure, psi
		q_i	Molar rate of component i , mole s ⁻¹
		r_w	Wellbore radius, ft
		S_{hmin}	Minimum horizontal stress, psi

✉ Yanli Pei
yanli.pei@utexas.edu

¹ Hildebrand Department of Petroleum and Geosystems Engineering, The University of Texas at Austin, Austin, TX 78712, USA

S_{Hmax}	Maximum horizontal stress, psi
\bar{S}_j	Saturation of phase j , fraction
\mathbf{t}	Prescribed traction on the boundary, psi
T	Transmissibility factor, mD-ft
\mathbf{u}	Displacement vector, ft
\mathbf{v}_j	Velocity of phase j , ft s ⁻¹
\mathbf{v}_s	Velocity of solid phase, ft s ⁻¹
V	Volume, ft ³
w_f	Fracture aperture, ft
x_{ij}	Mole fraction, fraction
α	Biot–Willis coefficient, dimensionless
γ_j	Specific gravity of phase j , lbf ft ⁻³
δ	Kronecker delta, dimensionless
ϵ	Strain tensor, dimensionless
μ_j	Viscosity of phase j , cp
ξ_j	Molar density of phase j , mole ft ⁻³
ρ	Mass density, lbf ft ⁻³
σ	Total stress tensor, psi
ϕ	Reservoir porosity, fraction
ϕ^*	True porosity, fraction
λ_j	relative mobility of phase j , cp ⁻¹

1 Introduction

Infill-well development has become a primary technique to increase hydrocarbon production for unconventional reservoirs (Miller et al. 2016; Lindsay et al. 2018; Guo et al. 2019). Extensive infill drilling in the producing layer, however, has caused too-close well spacing and severe fracture hits (King et al. 2017; Cipolla et al. 2018). Hence for multilayer unconventional reservoirs, placing an infill well (i.e., child well) in adjacent potential layers is preferred to enhance the ultimate recovery while mitigating the undesirable parent–child well interference (Sangnimmuan et al. 2019; Pei et al. 2021). Meanwhile, the performance of infill wells largely depends on the effectiveness of infill-well completion, which is mainly governed by the local principal stresses near the wellbore (Roussel et al. 2013; Safari et al. 2017; Suppachoknirun and Tutuncu 2017). Thus, a comprehension of the parent-well production induced 3D stress evolution under various geologic conditions is necessary for infill drilling in the field practice.

Many previous works focused on studying depletion-induced stress changes in single-layer reservoirs (Weng and Siebrits 2007; Gupta et al. 2012; Marongiu-Porcu et al. 2016; Pei et al. 2020). Based on the typical liquid-rich shale reservoir dataset, Roussel et al. (2013) investigated the occurrence and timing of S_{Hmax} reorientation between two fractured-horizontal wells following a period of production. They suggested completing infill wells prior to the onset time of stress reversal (i.e., a rotation of the local principal

stress direction by 90°) to ensure child fractures propagate more transversely and create a larger stimulated reservoir volume (SRV). Safari et al. (2017) also captured the stress alteration induced by tightly spaced horizontal-well production. Their main finding is that the perturbed stress field could significantly curve infill-well fractures, and the curving extent depends on bottomhole pressure, infill timing, stimulation design, etc. When the above studies mainly considered the depletion of uniform biwing fractures, Guo et al. (2018) simulated the magnitude and orientation change of principal stresses under nonuniform fracture geometries. In the meantime, Sangnimmuan et al. (2018) incorporated the nonplanar and slanted fracture geometry into their coupled flow and geomechanics simulation to evaluate the stress reorientation under different boundary conditions, fracture geometries, and differential stresses.

With the popularity of multilayer reservoir development, some studies on 3D stress evolution are underway (Defeu et al. 2019; Sangnimmuan et al. 2019). For example, Ajjisafe et al. (2017) employed an integrated reservoir and geomechanics model to investigate the production-associated spatiotemporal stress changes in a layered Delaware basin shale reservoir. As cross-layer stress interference was observed, they suggested landing child-well in an adjacent layer to avoid significant production loss. Likewise, Lin et al. (2018) integrated the reservoir simulation with geomechanics calculation to model the stress redistribution and hydraulic fracturing process in a multizone Montney formation. Li et al. (2020) also performed a field-scale geomechanical simulation to help identify the root cause of poor child-well performance in a stacked play of the Anadarko Basin. They found that the production-induced stress sink would attract infill-well fractures and cause severe fracture hits even with a staggered well layout. Although studies regarding stress evolution have progressed from 2 to 3D, their focus is more on a specific shale formation and lacks a comprehensive study of the stress responses under various reservoir and geomechanical settings.

In this work, we develop a 3D explicitly coupled geomechanics and multiphase compositional model with an embedded discrete fracture model (EDFM) and finite element method (FEM) to simulate the stress interference in a stacked unconventional reservoir. Different scenarios with and without interlayer geomechanical heterogeneity are investigated to cover a broad range of reservoirs and provide rules of thumb for the multilayer infill operations. Moreover, the mechanisms of stress reorientation or stress redistribution spreading towards the top and bottom potential pay zones have been systematically analyzed. The findings deliver an extensive understanding of the 3D stress evolution process and suggest the optimal strategy for infill drilling in the adjacent potential layers.

2 Mathematical Model

2.1 Multiphase Flow Model

Based on the strong form of the conservation statement (Lake 1989), the mass conservation equation for component i in a unit control volume is

$$\frac{\partial W_i}{\partial t} + \nabla \cdot \mathbf{F}_i - R_i = 0, \text{ for } i = 1, 2, \dots, n_c + 1, \quad (1)$$

where W_i is the accumulation rate of component i , \mathbf{F}_i is the net flux of component i , and R_i is the source term of component i , and n_c is the number of components.

Traditional fluid-flow models commonly assume a stationary solid phase, but in a deformable environment, we need to consider the deformation and movement of solid particles (Verruijt 1995; Pan 2009). There are mainly two different points: (1) the media porosity is changeable with time, so the true porosity (ϕ^*), defined as the pore volume to the bulk volume in the deformed configuration, other than traditional reservoir porosity (ϕ) should be used; (2) the solid phase is moveable, so the macroscopic interstitial velocity (\mathbf{v}^*), i.e., the real velocity of the fluid phase in the porous media, is different from the Darcy velocity (\mathbf{v}) by a solid velocity term. Upon these, we have the expressions for W_i , \mathbf{F}_i , and R_i as

$$W_i = \sum_{j=1}^{N_p} [\phi^* (\xi_j S_j x_{ij})], \quad \mathbf{F}_i = \sum_{j=1}^{N_p} [(\xi_j x_{ij}) \mathbf{v}_j^*], \quad R_i = \frac{q_i}{V_b}, \quad (2)$$

where N_p is the number of phases, ξ_j is the molar density of phase j , S_j is the saturation of phase j , x_{ij} is the mole fraction of component i in phase j , q_i is the molar rate of component i , V_b is the bulk volume of a gridblock.

Substituting Eq. (2) into Eq. (1) gives

$$V_b \frac{\partial}{\partial t} \sum_{j=1}^{N_p} [\phi^* (\xi_j S_j x_{ij})] + V_b \nabla \cdot \left\{ \sum_{j=1}^{N_p} [(\xi_j x_{ij}) \mathbf{v}_j^*] \right\} - q_i = 0, \text{ for } i = 1, 2, \dots, n_c + 1, \quad (3)$$

The mass balance equation of the solid phase is

$$\frac{D\phi^*}{Dt} = (1 - \phi^*) \nabla \cdot \mathbf{v}_s, \quad (4)$$

where $\frac{D}{Dt}(\cdot)$ is the material derivative, and it is defined as $\frac{D}{Dt}(\cdot) = \frac{\partial}{\partial t}(\cdot) + \mathbf{v}_s \cdot \nabla(\cdot)$.

The macroscopic interstitial velocity of phase j , \mathbf{v}_j^* , is related to the solid velocity \mathbf{v}_s as

$$\mathbf{v}_j^* = \phi^* S_j \mathbf{v}_s + \mathbf{v}_j, \quad (5)$$

After substituting Eqs. (4)–(5) into Eq. (3), we obtain the mass conservation equation in a deformable porous media as

$$V_b \frac{D[(1 + \varepsilon_v) \phi^* N_i^*]}{Dt} + V_b \nabla \cdot \left\{ \sum_{j=1}^{N_p} [(\xi_j x_{ij}) \mathbf{v}_j] \right\} - V_b \varepsilon_v \frac{D(\phi^* N_i^*)}{Dt} - q_i = 0, \text{ for } i = 1, 2, \dots, n_c + 1, \quad (6)$$

where ε_v is the volumetric strain, N_i^* is the number of moles for component i per pore volume, $N_i^* = \sum_{j=1}^{N_p} \xi_j S_j x_{ij}$, and the Darcy velocity of phase j is written as

$$\mathbf{v}_j = -\frac{k_{ij}}{\mu_j} \mathbf{k} \cdot (\nabla P_j - \gamma_j \nabla D), \quad (7)$$

where k_{ij} is the relative permeability of phase j , μ_j is the viscosity of phase j , \mathbf{k} is the permeability tensor, P_j is the pressure of phase j , γ_j is the specific gravity of phase j , and D is the depth from the datum plane.

If the small strain theory is assumed, i.e., $\|\varepsilon_v\| \ll 1$, the third term in Eq. (6) can be ignored; also, the material derivative can be approximated by its partial derivative, $\frac{D}{Dt}(\cdot) \approx \frac{\partial}{\partial t}(\cdot)$, when the solid velocity is negligibly small. Applying these two assumptions and substituting Darcy's law into Eq. (6) arrives at the final mass conservation equation

$$V_b \frac{\partial N_i}{\partial t} - V_b \nabla \cdot \left[\sum_{j=1}^{N_p} \xi_j x_{ij} \frac{k_{ij}}{\mu_j} \mathbf{k} \cdot (\nabla P_j - \gamma_j \nabla D) \right] - q_i = 0, \text{ for } i = 1, 2, \dots, n_c + 1, \quad (8)$$

where N_i is the number of moles for component i per bulk

volume, $N_i = \phi \sum_{j=1}^{N_p} \xi_j S_j x_{ij}$, ϕ is the reservoir porosity correlated with true porosity as $\phi = \phi^*(1 + \varepsilon_v)$.

We assume the fluid volume is a function of pressure and molar number, and the pore volume depends on pressure only (Chang 1990). The volume balance implies the volume occupied by all phases is equal to the total pore volume, thus

$$V_t(P, \mathbf{N}_i) = V_p(P), \quad (9)$$

where V_t is the total fluid volume, P is the pressure of the reference phase (usually oil phase), \mathbf{N}_i is a vector of the molar number for each component, and V_p is the pore volume.

Differentiating both sides of Eq. (9) with respect to time, applying the chain rule, and substituting Eq. (8) in the resulting equation gives the pressure equation as

$$\begin{aligned}
 &V_b \frac{\partial \phi}{\partial t} - \frac{\partial V_t}{\partial P} \frac{\partial P}{\partial t} - V_b \sum_{i=1}^{n_c+1} \bar{V}_{ti} \nabla \cdot \sum_{j=1}^{N_p} \left(\xi_j x_{ij} \frac{k_{tj}}{\mu_j} \mathbf{k} \cdot \nabla P \right) \\
 &= V_b \sum_{i=1}^{n_c+1} \bar{V}_{ti} \nabla \cdot \sum_{j=1}^{N_p} \left[\xi_j x_{ij} \frac{k_{tj}}{\mu_j} \mathbf{k} \cdot (\nabla P_{c2j} - \gamma_j \nabla D) \right] + \sum_{i=1}^{n_c+1} \bar{V}_{ti} q_i,
 \end{aligned}
 \tag{10}$$

where P_{c2j} is the capillary pressure between phase j and the reference phase, \bar{V}_{ti} is the partial derivative of the total fluid volume to the molar number of component i ,

$$\bar{V}_{ti} = \left(\frac{\partial V_t}{\partial N_i} \right)_{P, N_{k(k \neq i)}}, \tag{11}$$

2.2 Geomechanics Model

Consider a continuum body Ω with a fracture discontinuity Γ_f , as shown in Fig. 1. Based on linear momentum balance, the static equilibrium equation of the whole system can be written as

$$\nabla \cdot \boldsymbol{\sigma} + \rho \mathbf{b} = 0, \tag{12}$$

where $\boldsymbol{\sigma}$ denotes the total stress tensor, ρ is the total mass density, and \mathbf{b} is the body force.

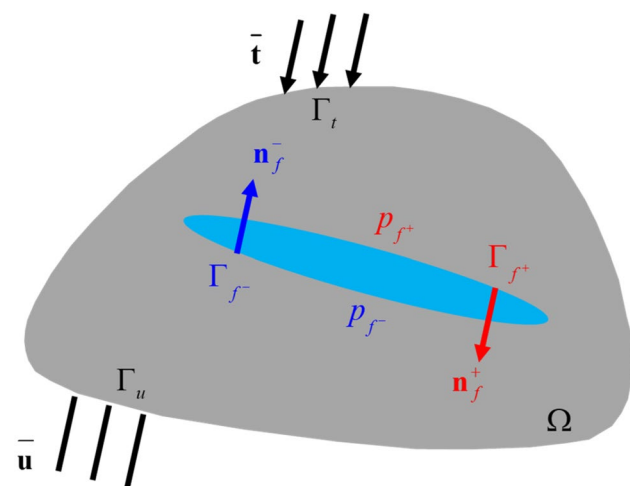


Fig. 1 A sketch of a fractured porous media and the associated boundary conditions

Biot’s theory (1941, 1955) is commonly used to describe the poroelastic effect in linear isotropic poroelastic material. In this work, it is adopted to approximate the mechanical deformation of the reservoir rock. With negative compressive stresses as the sign convention, the stress–strain relation is expressed as

$$\boldsymbol{\sigma} - \boldsymbol{\sigma}_0 = \mathbf{D} : \boldsymbol{\varepsilon} - \alpha (p - p_0) \boldsymbol{\delta}, \tag{13}$$

where \mathbf{D} is the stiffness tensor, $\boldsymbol{\varepsilon}$ is the strain tensor, α is the Biot–Willis coefficient, $\boldsymbol{\delta}$ is the Kronecker delta, $(\cdot)_0$ is the property at the reference state, and p is the effective average pore pressure,

$$p = \sum_{j=1}^{N_p} S_j P_j, \tag{14}$$

Since small strain theory is assumed, the strain tensor is written as the symmetric gradient of the displacement vector

$$\boldsymbol{\varepsilon} = \frac{1}{2} (\nabla \mathbf{u} + \nabla^T \mathbf{u}), \tag{15}$$

where \mathbf{u} is the displacement vector, $\mathbf{u} = (u_x, u_y, u_z)^T$.

Combining Eqs. (12)–(15) obtains the final system of geomechanical governing equations. The essential and natural boundary conditions of the fractured porous media are defined as

$$\begin{aligned}
 &\mathbf{u} = \bar{\mathbf{u}}, \text{ on } \Gamma_u \\
 &\boldsymbol{\sigma} \cdot \mathbf{n} = \bar{\mathbf{t}}, \text{ on } \Gamma_t \\
 &\boldsymbol{\sigma} \cdot \mathbf{n}_f = -p_f \cdot \mathbf{n}_f, \text{ on } \Gamma_f,
 \end{aligned}
 \tag{16}$$

where $\bar{\mathbf{u}}$ is the prescribed displacement on the displacement boundary Γ_u , $\bar{\mathbf{t}}$ is the prescribed traction on the traction boundary Γ_t , \mathbf{n} is the outward unit normal vector to the external boundary $\partial\Omega$ where $\Gamma_u \cap \Gamma_t = 0$ and $\Gamma_u \cup \Gamma_t = \partial\Omega$, p_f is the fluid pressure in the fracture, and \mathbf{n}_f is the unit normal vector to the internal boundary Γ_f with $\mathbf{n}_f = \mathbf{n}_f^- = -\mathbf{n}_f^+$.

Once the unknowns $(\mathbf{u}, \boldsymbol{\varepsilon}, \boldsymbol{\sigma})$ in the geomechanics model are solved, the coupling parameters from the geomechanics calculation to the fluid-flow model, such as porosity and permeability, need to be updated. The formulation of the true porosity, ϕ^* , is directly derived from the solid mass balance in Eq. 4 (Chin et al. 2000; Haddad and Sepehrnoori 2017). In addition, the gradient of solid velocity, $(\nabla \cdot \mathbf{v}_s)$, can be expressed in terms of the volumetric strain, ε_v , as

$$\nabla \cdot \mathbf{v}_s = \nabla \cdot \frac{\partial \mathbf{u}}{\partial t} = \frac{\partial (\nabla \cdot \mathbf{u})}{\partial t} = \frac{\partial \varepsilon_v}{\partial t}, \tag{17}$$

Substituting Eq. (17) into Eq. (4) and integrating both sides from time 0 to t arrives at

$$\phi^* = 1 - (1 - \phi_0)e^{-\epsilon_v}, \tag{18}$$

where ϕ_0 is the reservoir porosity at the reference state.

From the definition of volumetric strain, we obtain the relation between the reservoir porosity and true porosity as

$$\phi = \phi^*(1 + \epsilon_v), \tag{19}$$

The reservoir permeability can be related to different state variables, such as fluid pressure, porosity, mean normal stress, shear stress, and axial strain (Raghavan and Chin 2002; Zhang et al. 2007; Wang and Sharma 2019). Here, we update the reservoir permeability based on the change of true porosity

$$k = k_0 \left(\frac{\phi^*}{\phi_0^*} \right)^m, \tag{20}$$

where k and k_0 are the permeability in a specific direction (i.e., x -, y -, or z -direction) at current and reference states, ϕ^* and ϕ_0^* are the current and reference true porosity, and m is the empirical power-law exponent after David et al. (1994).

3 Numerical Model

3.1 Discretization Scheme

The finite volume method (FVM) is used to discretize the multiphase compositional model with EDFM incorporated to characterize the fluid flow through complex fractures. The basic idea of EDFM (Li and Lee 2008; Moinfar et al. 2014; Xu et al. 2017) is to discretize the reservoir with structured grids, introduce additional grids for fracture segments, and connect non-neighboring cells by the definition of non-neighboring connections (NNCs). As shown in Fig. 2, each

fracture is cut into small segments by the boundaries of matrix gridblocks, and the fracture gridblocks have the same grid size as the matrix cells in the computational domain. For each fracture cell, the volume of the fracture segment is calculated from

$$V_f = S_{\text{seg}} w_f, \tag{21}$$

where S_{seg} is the area of the fracture segment perpendicular to the fracture aperture and w_f is the fracture aperture. The pore volume of the fracture cell is assigned as

$$\phi_f = \frac{S_{\text{seg}} w_f}{V_b}, \tag{22}$$

where ϕ_f is the effective porosity of the fracture cell and V_b is the bulk volume of cell assigned to the fracture segment.

In the discretized form, the mass flux of phase j between two cells in a NNC pair (i.e., matrix–fracture connection or fracture–fracture connection) can be generalized as

$$Q_j = \rho_j \lambda_j T_{\text{NNC}} \Delta \Phi_j, \tag{23}$$

where ρ_j is the mass density of phase j , λ_j is the relative mobility of phase j , T_{NNC} is the NNC transmissibility factor, and $\Delta \Phi_j$ is the potential difference between two cells.

Three types of NNCs are defined in EDFM to represent the flow communication between physically connected but non-neighboring cells (Sepehrnoori et al. 2020). The transmissibility factors between matrix and fracture segment, T_{f-m} , between fracture segments in an individual fracture, T_{f-f}^s , and between intersecting fracture segments, T_{f-f}^i , can be expressed as

$$T_{f-m} = \frac{2A_f (\mathbf{k} \cdot \mathbf{n}_f) \cdot \mathbf{n}_f}{d_{f-m}}, \tag{24}$$

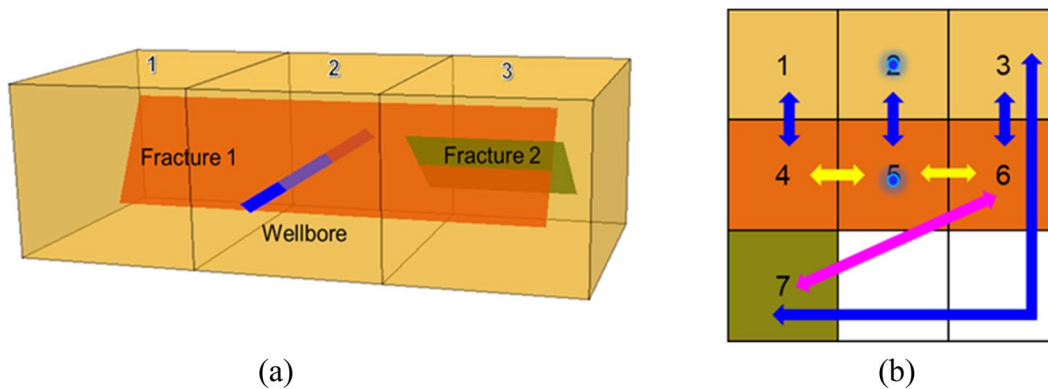


Fig. 2 Illustration of **a** physical domain and **b** computational domain for fractured porous media with EDFM. Three fracture cells (4, 5, and 6) are introduced to represent Fracture 1, and one fracture cell (7) is introduced for Fracture 2. The blue arrows represent the matrix–frac-

ture connection, the yellow arrows represent the fracture–fracture connection in an individual fracture, and the magenta arrow represents the fracture–fracture connection of two intersecting fractures

$$T_{f-f}^s = \frac{T_{f1}^s T_{f2}^s}{T_{f1}^s + T_{f2}^s}, T_{f1}^s = \frac{k_f A_c}{d_{s1}}, T_{f2}^s = \frac{k_f A_c}{d_{s2}}, \tag{25}$$

$$T_{f-f}^i = \frac{T_{f1}^i T_{f2}^i}{T_{f1}^i + T_{f2}^i}, T_{f1}^i = \frac{k_{f1} w_{f1} L_i}{d_{f1}}, T_{f2}^i = \frac{k_{f2} w_{f2} L_i}{d_{f2}}, \tag{26}$$

where A_f is the area of the fracture segment on one side, d_{f-m} is the average normal distance from the matrix to fracture, k_f is the fracture permeability, A_c is the common area for two neighboring segments, d_{s1} and d_{s2} are distances from the centroids of segments 1 and 2 to the common face, k_{f1} and k_{f2} are the permeability of fracture segments 1 and 2, w_{f1} and w_{f2} are the aperture of fracture segments 1 and 2, L_i is the intersection length of two fracture segments, and d_{f1} and d_{f2} are the weighted average of the normal distance from the centroids of the fracture segments 1 and 2 to the intersection line.

The effective well index, WI_f , models the well-fracture intersections (Moinfar et al. 2013) as

$$WI_f = \frac{2\pi k_f w_f}{\ln\left(0.14\sqrt{L^2 + H^2}/r_w\right)}, \tag{27}$$

where L is the length of the fracture segment, H is the height of the fracture segment, and r_w is the wellbore radius.

The geomechanics model is discretized using the finite element method (FEM) with linear hexahedron elements. To derive the weak form of the equilibrium equation, we multiply Eq. (12) by an admissible test function $\delta \mathbf{u}$ in the Sobolev space, integrate the product over the computational domain, and apply the divergence theorem

$$\int_{\Omega} \nabla \delta \mathbf{u} : \mathbf{D} : \boldsymbol{\varepsilon} d\Omega - \int_{\Omega} \nabla \delta \mathbf{u} : \alpha p \mathbf{m} d\Omega = \int_{\Omega} \delta \mathbf{u} \cdot \boldsymbol{\rho} b d\Omega + \int_{\Gamma_t} \delta \mathbf{u} \cdot \bar{\mathbf{t}} d\Gamma + \int_{\Gamma_f} [[\delta \mathbf{u}]] p_f \cdot \mathbf{n}_f d\Gamma, \tag{28}$$

where \mathbf{m} is the vector of Dirac delta function defined as $\mathbf{m} = (1, 1, 0)^T$ for 2D problems and $\mathbf{m} = (1, 1, 1, 0, 0, 0)^T$ for 3D problems, and $[[\mathbf{u}]] = \mathbf{u}^+ - \mathbf{u}^-$ is the displacement jump over fracture faces.

In this work, hydraulic fractures are assumed well-propped by high-concentration or high-strength proppants, so the fracture aperture change becomes negligible and barely affects the stress evolution (Sangnimmuan et al. 2018; Liu et al. 2020). Hence, the last term in Eq. (28) is neglected at this stage, and the fracture effect on the matrix deformation will be reflected through pore pressure changes of the matrix gridblocks intersected by the fracture segments. The dynamic change of fracture aperture under poorly propped

conditions, which is beyond the scope of this work, will be considered in our future model development.

The displacement unknown (\mathbf{u}) and strain unknown ($\boldsymbol{\varepsilon}$) in Eq. (28) can be approximated by multiplying the nodal values and shape functions as

$$\mathbf{u} = \mathbf{N}\underline{\mathbf{u}}, \quad \boldsymbol{\varepsilon} = \mathbf{B}\underline{\mathbf{u}}, \tag{29}$$

where \mathbf{N} is the shape function vector, \mathbf{B} is the strain–displacement matrix, and $\underline{\mathbf{u}}$ is the nodal displacement vector.

By substituting Eq. (29) back into Eq. (28), we obtain the discretized geomechanics model as

$$\mathbf{K}\underline{\mathbf{u}} - \mathbf{Q} = \mathbf{F}, \tag{30}$$

where

$$\mathbf{K} = \int_{\Omega} \mathbf{B}^T \mathbf{D} \mathbf{B} d\Omega, \tag{31}$$

$$\mathbf{Q} = \int_{\Omega} \mathbf{B}^T \alpha p \mathbf{m} d\Omega, \tag{32}$$

$$\mathbf{F} = \int_{\Gamma_t} \mathbf{N}^T \bar{\mathbf{t}} d\Gamma + \int_{\Omega} \mathbf{N}^T \boldsymbol{\rho} b d\Omega, \tag{33}$$

3.2 Solution Procedure

In this work, an explicitly coupling approach is implemented to solve our 3D coupled geomechanics and multiphase compositional model. As shown in Fig. 3, both flow and geomechanics models are initialized with their original inputs at time zero. For each timestep, the gridblock pressure is solved implicitly where EDFM is incorporated to represent complex discrete fractures. The mass conservation equation is then solved explicitly for the overall molar concentration of each component. Flash calculations compute the phase compositions using the Peng–Robinson equation of state (Peng and Robinson 1976), then evaluate phase saturations from phase molar amounts and molar densities. Once the flow problem is solved, the updated pressure and saturations are transferred to the FEM-based geomechanics model to calculate the nodal displacement values. The strain and stress tensors in each element are then computed by mapping the nodal displacements to the grid center with a group of shape functions. Finally, the reservoir porosity and permeability are updated based on the resultant volumetric strain and returned to the fluid-flow model for the next timestep simulation. The coupling procedure is repeated until the maximum simulation time is reached. To be noted, as small timesteps are applied to ensure the stability and convergence of the implicit–pressure, explicit–concentration algorithm, the explicitly coupled procedure presented in this work is still

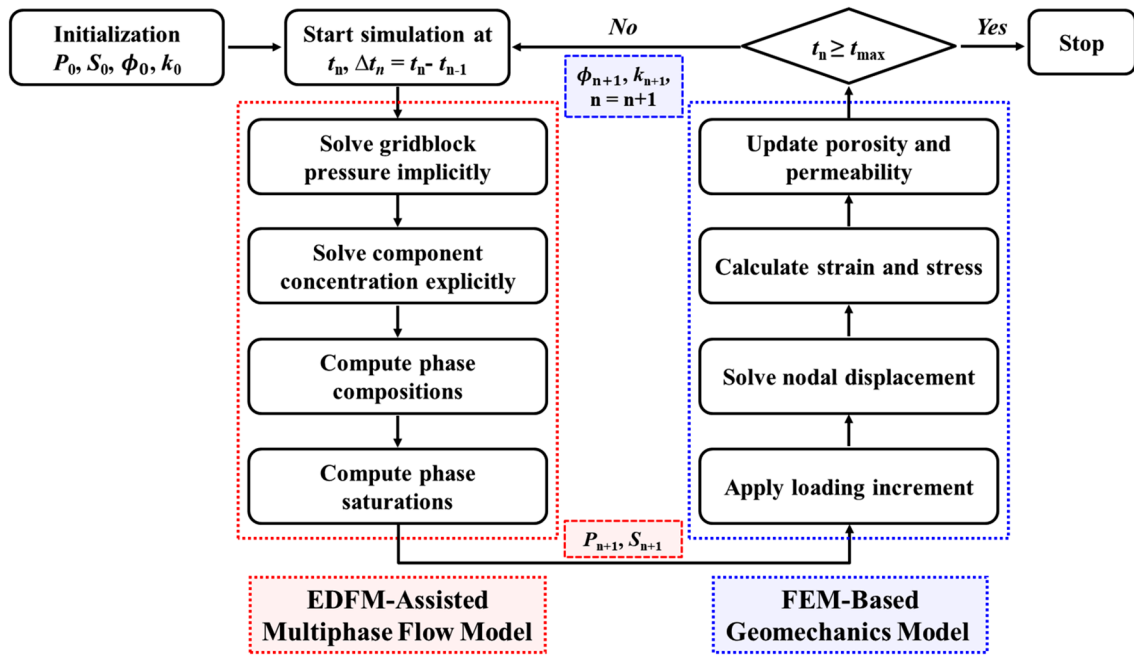


Fig. 3 Flow diagram of explicitly coupled geomechanics and multiphase compositional model

Table 1 Parameters used in the McNamee–Gibson problem

Parameter	Value	Unit
Porosity	0.2	–
Permeability	1000	mD
Young’s modulus	1.0	GPa
Poisson’s ratio	0	–
Biot–Willis coefficient	1	–
Fluid viscosity	1.0	mPa s
Load q	1.0	psi
Load range a	3.28	ft

comparable to some iteratively coupled methods (Haddad and Sepehrnoori 2017).

4 Validation

4.1 McNamee–Gibson Problem

The McNamee–Gibson problem (1960a, b) describes the plane strain consolidation in a poroelastic half space. Table 1 summarizes the parameters used in this validation problem. A uniform load is applied instantaneously over a strip of width $2a$, which leads to immediate changes in the pressure and deformation fields. Because of the symmetry of the domain with $x=0$, only the right half of the plane is considered in the simulation. The geometry and boundary

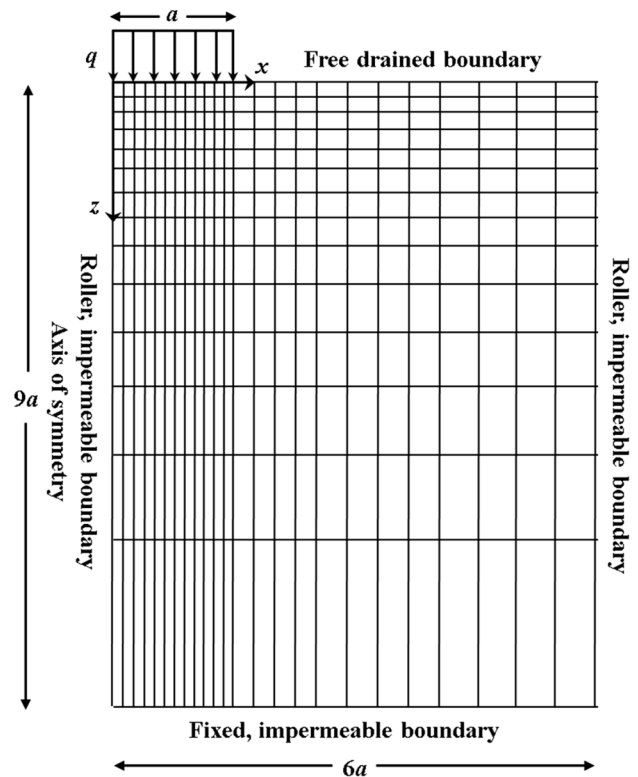


Fig. 4 Grid mesh and boundary conditions for the McNamee–Gibson problem

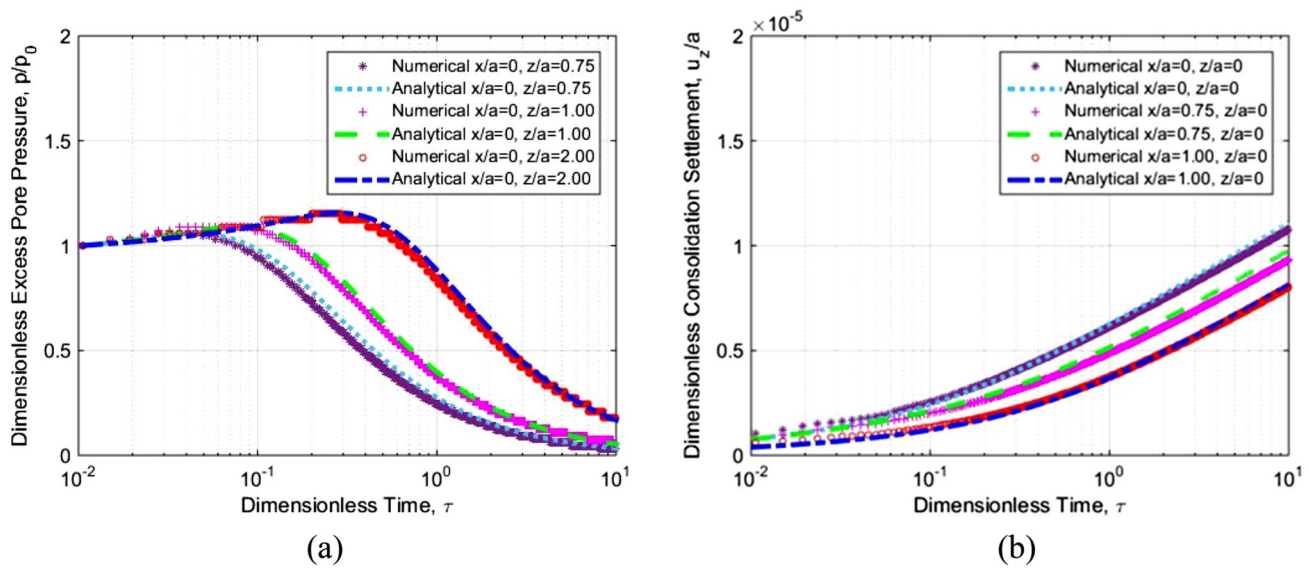


Fig. 5 Comparison of numerical and analytical solutions for the McNamee–Gibson problem for **a** excess pore pressure and **b** consolidation settlement. p_0 is the initial excess pore pressure induced by the Skempton effect, and τ is the dimensionless time defined as $\tau = ct/a^2$

conditions are shown in Fig. 4. A nonuniform grid mesh is used with fine grids over the loading region and coarse grids away from the x centerline. The zero normal displacement is applied on the left and right edges, and the bottom edge is fixed in both x - and z -direction. The fluid is only allowed to flow out from the top boundary, and other boundaries are impermeable.

The detailed analytical solution is provided in “Appendix A”. Figure 5 compares numerical and analytical solutions for excess pore pressure and consolidation settlement at different locations. Initially, the Skempton effect, i.e., pore pressure generation because of the load q , is observed due to the extremely short, undrained loading process. After a while, the Mandel–Cryer effect, which refers to an instant increase of the pore pressure at the middle of the domain, is captured by our model from the two-way coupling between fluid flow and solid deformation. For example, an approximately 10% rise in the excess pore pressure is observed for point ($x = 0, z = a$) at $\tau = 0.08$. The surface settlement varies with x -location due to the imposition of a strip load over a limited width a . The closer to the symmetry plane ($x = 0$), the larger the consolidation settlement. Our model produces rather similar results when compared with the analytical solutions at both early and late times, which verifies our coupled flow and geomechanics model.

4.2 Single-Fracture Problem

A single-fracture model is built to validate the implementation of EDFM in our coupled model. The local grid refinement (LGR) serves as the benchmark in this part.

Table 2 Parameters used in the single-fracture problem

Parameter	Value	Unit
Matrix porosity	0.1	–
Matrix permeability	0.1	mD
Fracture aperture	0.01	ft
Fracture permeability	10,000	mD
Young’s modulus	6.89	GPa
Poisson’s ratio	0.3	–
Biot–Willis coefficient	1	–
Fluid viscosity	1.0	mPa s
Initial pressure	3000	psi
Bottomhole pressure	1000	psi
Total stress in x direction	3400	psi
Total stress in y direction	3500	psi
Total stress in z direction	4000	psi

The reservoir dimensions are 410 ft \times 410 ft \times 80 ft. In the EDFM model, a uniform 41 \times 41 \times 1 matrix grid is used. The fracture has a width of 0.01 ft and a conductivity of 100 mD-ft. In the LGR model, the parent cells containing the fracture segment are refined into 5 \times 1 \times 1 subgrids. The fracture width is equal to the dimension of the center refinement, which is 0.01 ft. Zero normal displacement boundary conditions are applied to the lateral and bottom edges, except for the top boundary in the z -direction with a 4,000 psi traction stress. More details about the model parameters can be found in Table 2.

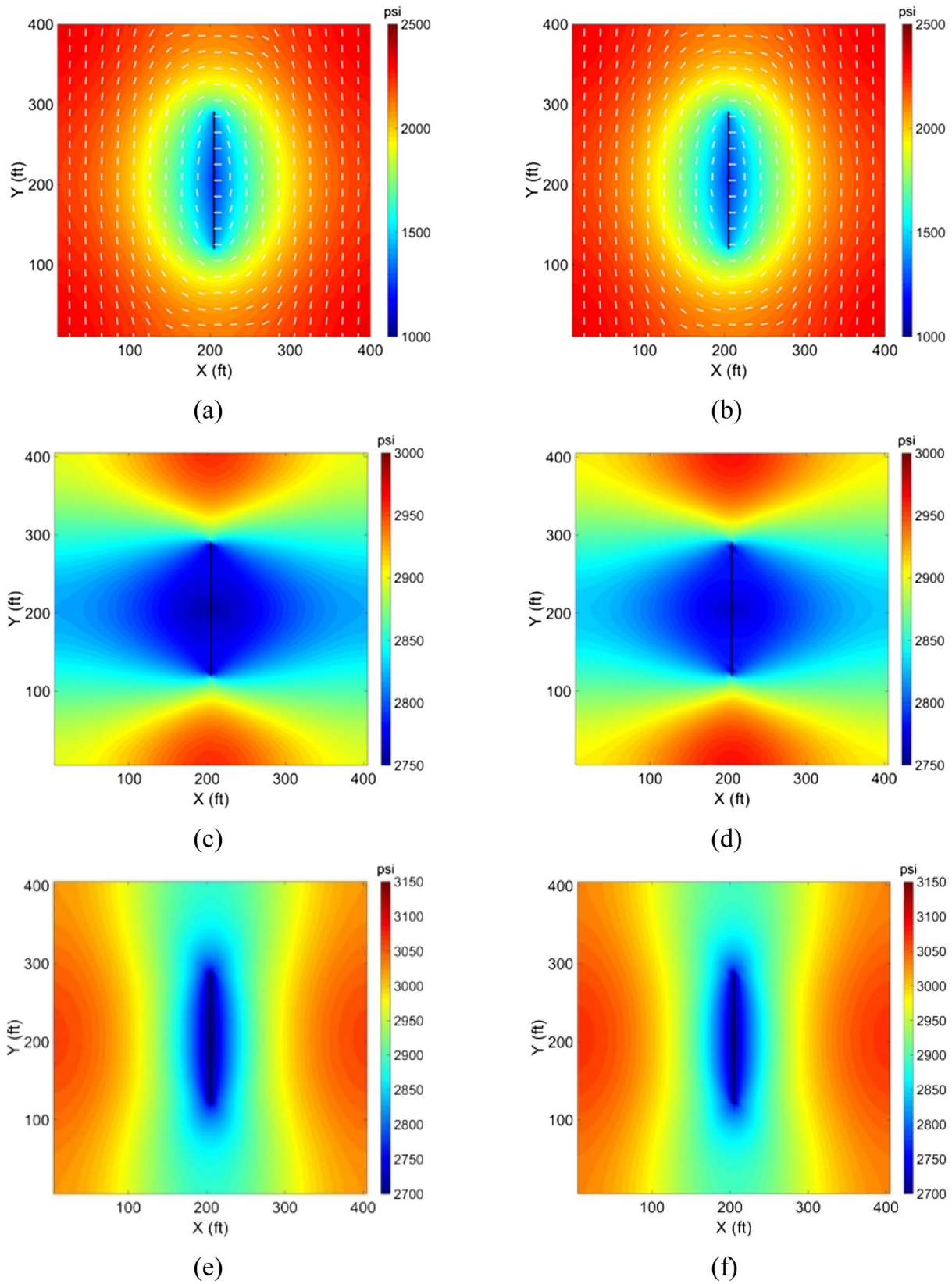


Fig. 6 Comparison between LGR and EDFM after 50 days of production for **a** pressure distribution (contours) and orientation of S_{Hmax} (white lines) for LGR; **b** pressure distribution (contours) and orien-

tation of S_{Hmax} (white lines) for EDFM; **c** S_{xx} distribution (contours) for LGR; **d** S_{xx} distribution (contours) for EDFM; **e** S_{yy} distribution (contours) for LGR; **f** S_{yy} distribution (contours) for EDFM

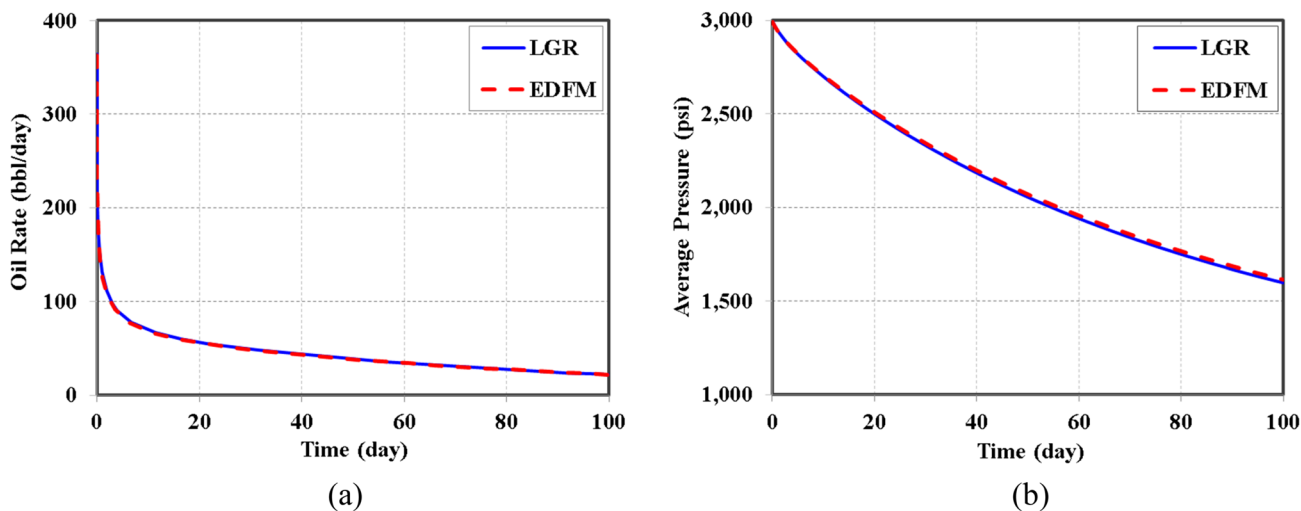


Fig. 7 Comparison of a oil rate and b average pressure between LGR and EDFM

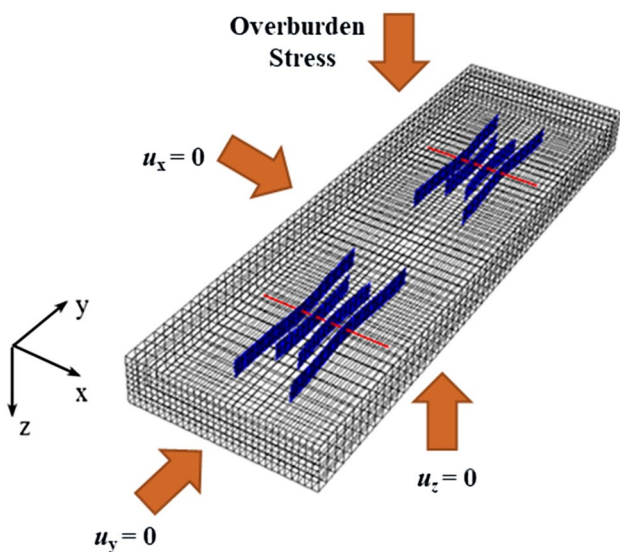


Fig. 8 3D reservoir geometry with two well segments and boundary conditions

A comparison between LGR and EDFM is shown in Fig. 6 for pore pressure with S_{Hmax} orientation, total stress in the x - and y -direction. Owing to the elliptical depletion area around the fracture, the stress change rates in x - and y -direction are different, resulting in the reorientation of the local principal stresses. The initial orientation of S_{Hmax} is in the y -direction, and it rotates toward the x -direction around fracture tips after 50 days of production. There is nearly no difference in the total stress distribution between LGR and EDFM models. Higher S_{xx} occurs at the top and bottom regions to support pressure depletion in the x -direction, whereas higher S_{yy} occurs at the left and right areas to support pressure depletion in the y -direction. Also, the oil rate

Table 3 Rock properties of different layers

Formation	Thickness, ft	ϕ , fraction	k_m , nD	Type
Top layer	30	0.1	500	Potential
Interlayer	20	0.05	10	Interlayer
Middle layer	60	0.1	500	Production
Interlayer	20	0.05	10	Interlayer
Bottom layer	30	0.1	500	Potential

and average pressure calculated from the EDFM match well with LGR results, as shown in Fig. 7. The good agreement in pressure distribution, stress field, and production profile confirms the validity of implementing EDFM in our coupled model.

5 Case Studies

A five-layer fractured reservoir model is established following a dataset in Sangnimmun et al. (2019). As shown in Fig. 8, the reservoir dimensions in the x -, y -, and z -direction are 600 ft, 2000 ft, and 160 ft, respectively, meshed into 30, 50, and 7 gridblocks in each direction. Vertically, the production target is discretized into 3 rows, while other targets are each discretized into 1 row. Table 3 lists detailed layer thickness, porosity, permeability, and type. Two horizontal wells with a 1000 ft distance in-between are drilled in the middle production layer. Each well has four nonplanar hydraulic fractures that are simulated with stress shadow effect included using an in-house hydraulic fracture model (Wu and Olson 2015; Wang et al. 2020; Wang and Olson 2021). The prospective infill well will be staggered either in the top or bottom potential layer. A two-phase fluid flow

Table 4 Summary of reservoir parameters

Parameter	Value	Unit
Reservoir depth	8000	ft
Initial reservoir pressure	6000	psi
Bottomhole pressure	2000	psi
Oil viscosity	1.0	mPa s
Water viscosity	0.8	mPa s
Water saturation	0.2	–
Young's modulus	30	GPa
Poisson's ratio	0.3	–
Biot–Willis coefficient	0.9	–
Fracture conductivity	150	mD-ft
Fracture spacing	50	ft
Inner-fracture half length	190	ft
Outer-fracture half length	310	ft
Initial stress in x direction	6700	psi
Initial stress in y direction	7000	psi
Initial stress in z direction	8000	psi

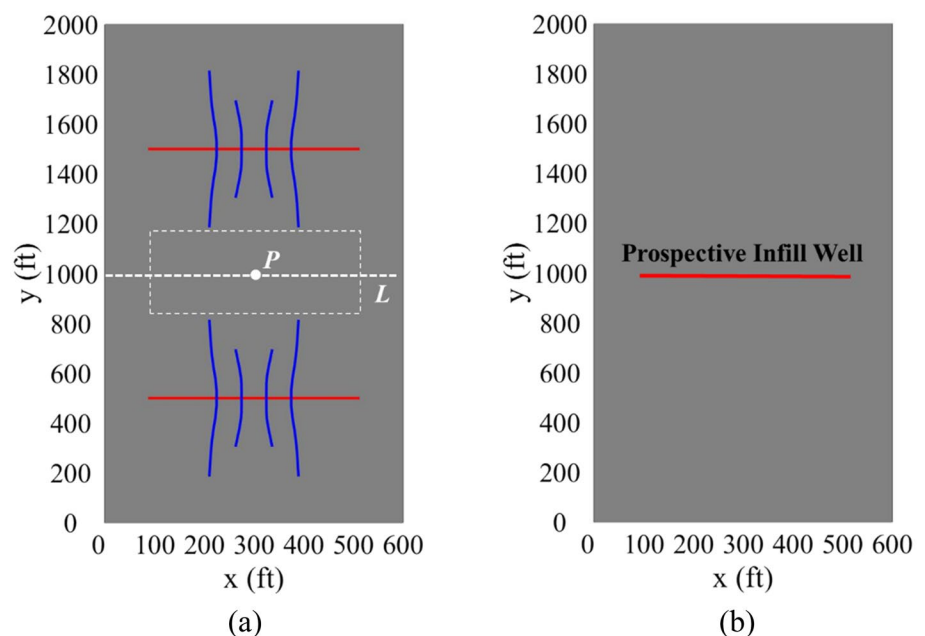
(i.e., oil and water) is modeled, and Peaceman's model is used to calculate the flux between the horizontal wellbore and the hosting gridblock. The reservoir has an 8000 psi overburden stress from the top, zero normal displacement on the lateral and bottom boundaries, and no-flow boundaries at all faces. Table 4 summarizes the properties of the reservoir model. In our 10-year simulation runs, the initial timestep is set as $1e-5$ days, and the automatic timestep strategy (Mehra et al. 1982; Chang 1990) is employed with an upper bound of 2 days.

In the first part, we keep the homogeneity among the top, middle, and bottom layers but change the reservoir permeability and fracture penetration to investigate their impacts on the stress evolution. Since microseismic and log data indicate that many stratified unconventional reservoirs honor different mechanical properties among layers (Thiercelin and Plumb 1994; Ferrill et al. 2014; Yue et al. 2019), the heterogeneity of differential stress and rock stiffness over depth is included in the second part to determine their effects on the stress interference of a multilayer reservoir. As shown in Fig. 9, we choose an observation line L along the infill location and an observation point P at the center of the infill region to track the spatial and temporal stress changes, respectively. Although line L and point P are only marked on the middle production layer in Fig. 9, we also project these specific locations vertically to the top and bottom targets for stress evolution analysis. The optimal infill strategy can be determined by monitoring the orientation and magnitude of S_{Hmax} and S_{Hmin} , respectively.

5.1 Effect of Reservoir Permeability

In this section, the effects of reservoir permeability (k_m) on stress evolution and infill drilling are investigated. We keep the interlayer permeability at 10 nD and vary the permeability of the top, middle, and bottom targets simultaneously from 100 to 1000 nD. The fractures are constrained within the middle production target. Figure 10 provides a comparison between 200 and 700 nD cases for the orientation and magnitude changes after 5 years of production. The orientation change of S_{Hmax} in the 200 nD case is mainly constrained within the top potential and middle production

Fig. 9 **a** Well and fracture configuration in the production layer and **b** location of prospective infill well in the top and bottom potential layers. The observation line L along the infill location and the observation point P at the center of the infill region are marked in the production layer but projected vertically to the top and bottom targets for stress evolution analysis



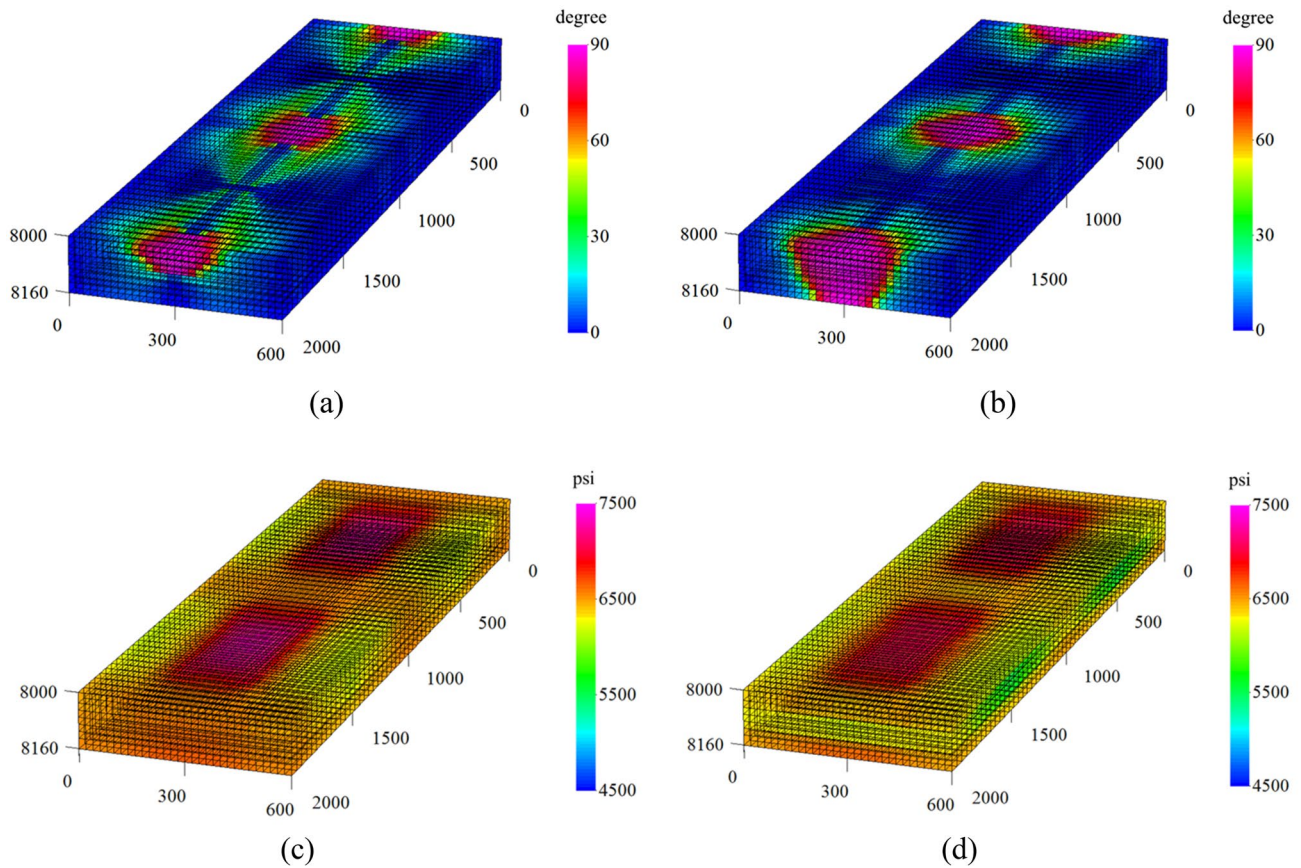


Fig. 10 Comparison between $k_m=200$ nD and $k_m=700$ nD after 5 years for **a** orientation change of S_{Hmax} at $k_m=200$ nD, **b** orientation change of S_{Hmax} at $k_m=700$ nD, **c** magnitude distribution of S_{hmin} at $k_m=200$ nD, and **d** magnitude distribution of S_{hmin} at $k_m=700$ nD

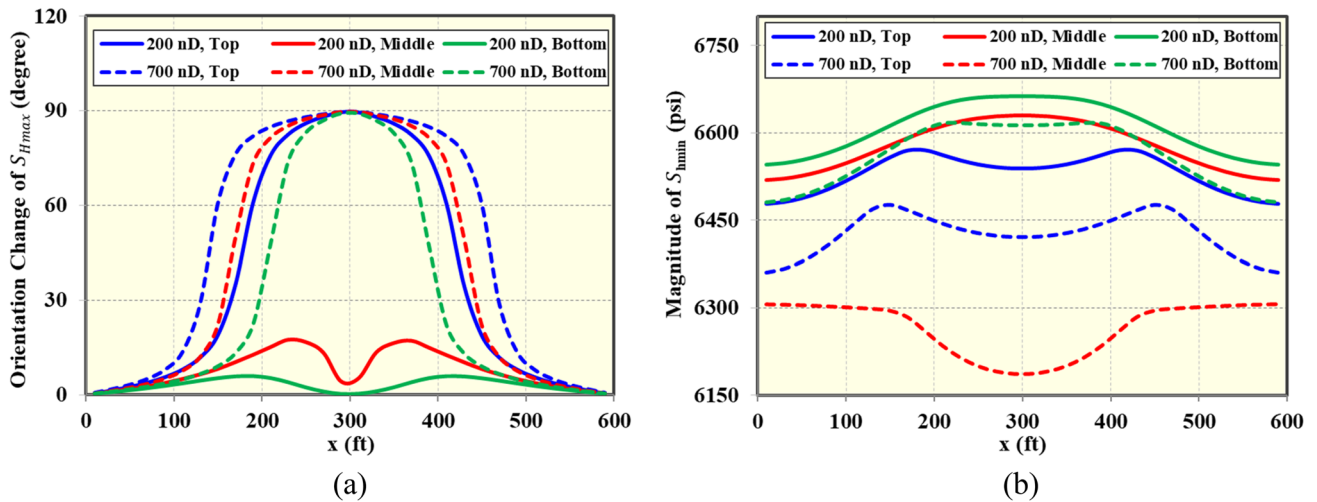


Fig. 11 **a** Orientation change of S_{Hmax} and **b** magnitude variation of S_{hmin} along prospective infill line at 5 years of parent-well production under different reservoir permeabilities

targets, as shown in Fig. 10a. In contrast, Fig. 10b shows the orientation change of S_{Hmax} in the 700 nD case has

propagated throughout all three target layers. Besides, a lower permeability leads to slower but more even pressure

depletion in adjacent potential layers. Thus, we notice an expanded area of stress reorientation in the top layer of the 200 nD case as compared to the 700 nD case. On the other hand, a high reservoir permeability results in significant pressure drops over the SRV-projected region in adjacent layers, which would greatly reduce the magnitude of S_{hmin} , as in Fig. 10c and d. Within the SRV and SRV-projected region, the drainage rate along the x -direction is much faster than that along the y -direction (i.e., the initial direction of S_{Hmax}) at late times, and it is more significant in the high-permeability reservoir. Therefore, the stress in the y -direction maintains the maximum horizontal stress most of the time, and barely any S_{Hmax} reorientation in the fractured area can be observed.

At 5 years of parent-well production, the orientation change of S_{Hmax} is analyzed along with the prospective infill lines, as shown in Fig. 11a. For the 200 nD case, a significant orientation change of S_{Hmax} only occurs in the top layer (i.e., solid blue line), and the orientation change of S_{Hmax} in the middle and bottom layers is limited under 20° (i.e., solid red and green lines). The larger orientation change of S_{Hmax} is attributed to the faster depletion along the top-layer infill line under the gravity effect. It also corresponds to a lower magnitude of S_{hmin} along with the prospective infill well (i.e., solid blue line), as shown in Fig. 11b. When the reservoir permeability is increased to 700 nD, all three layers experience a greater S_{Hmax} reorientation or even S_{Hmax} reversal. The range affected by stress rotation is 300 ft and 150 ft, respectively, along the infill line in the top and bottom layers. Also, increasing reservoir permeability by 500 nD leads to a 120 psi S_{hmin} drop at the top-layer center, but only a 50 psi drop at the bottom-layer center. These results indicate that a high reservoir permeability will induce more

significant stress reorientation for all layers and a relatively larger S_{hmin} drop in the top layer.

To achieve a satisfactory infill-well completion, we should follow two things: (1) fracturing the infill well prior to the critical time of stress reversal (CTSR) as a 90° of stress reorientation at the infill location inhibits the transverse propagation of child fractures; (2) monitoring the temporal evolution of S_{hmin} to avoid undesirable fracture growth toward depletion-induced stress sink. Figure 12a summarizes the influence of reservoir permeability on the CTSR from five tested cases—CTSR at the layer center goes down exponentially as the reservoir permeability increases, and the top layer always has an earlier stress reversal than the two other layers. The findings suggest that stress reorientation should be emphasized when infill drilling is needed in a high-permeability reservoir. Moreover, if the infill well is to be placed in the top layer, rigorous stress modeling is recommended before actual field operations. Figure 12b shows the S_{hmin} change over time at the top- and bottom-layer center. Although there is no significant variation of S_{hmin} before the CTSR, a higher permeability leads to much faster stress depletion. In addition, the top layer corresponds to a much smaller S_{hmin} as compared to the bottom layer.

5.2 Effect of Fracture Penetration

Weak bedding interfaces or stress barriers trigger the hydraulic fracture penetration into adjacent layers (Cai 2013; Tang et al. 2018; Mehrabi et al. 2021). In the previous cases, fractures are perfectly contained by the production layer. In the following cases, the fracture height (h_f) varies from no penetration to 10 ft upward penetration, 20 ft upward penetration, 10 ft downward penetration, and 20 ft downward penetration. Other parameters remain the same, as presented

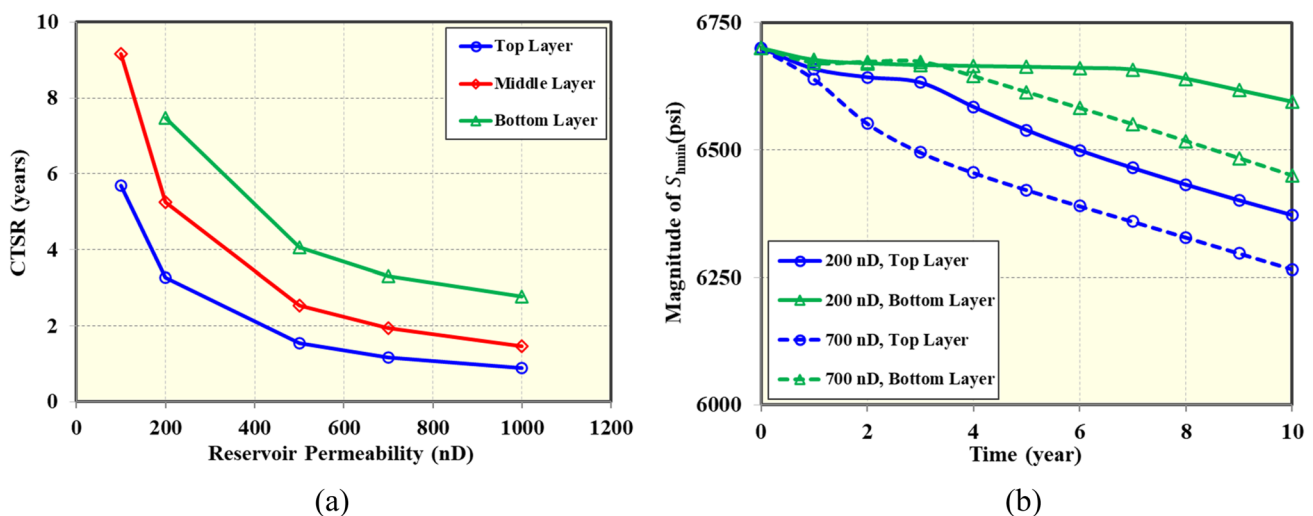


Fig. 12 **a** Effect of reservoir permeability on CTSR and **b** temporal variation of S_{hmin} . All values are evaluated at the layer center

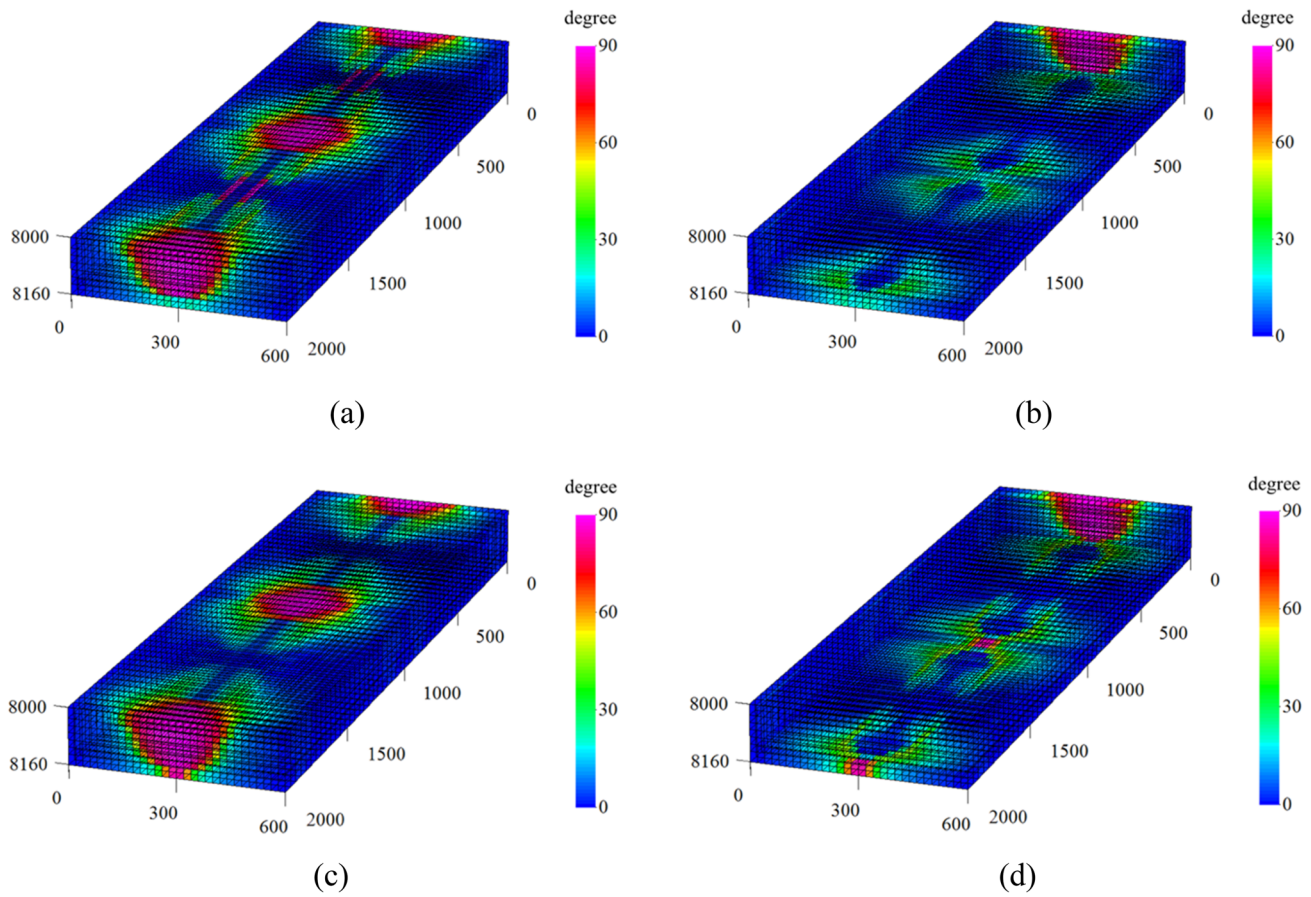


Fig. 13 Orientation change of S_{Hmax} at the top and bottom layers for **a, b** $h_f=20$ ft (upward penetration) and **c, d** $h_f=-20$ ft (downward penetration) after 3.5 years. Top view: **(a, c)**; bottom view **(b, d)**

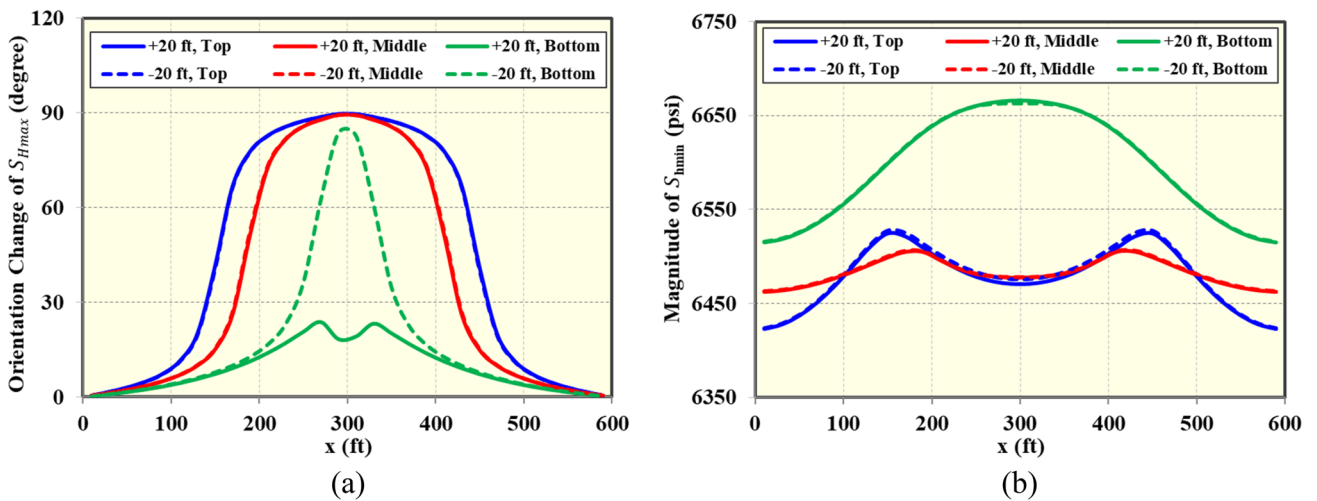


Fig. 14 a Orientation change of S_{Hmax} and **b** magnitude variation of S_{hmin} along prospective infill line at 3.5 years of parent-well production under different fracture penetrations

in Tables 3 and 4. Figure 13 shows the orientation change of S_{Hmax} at the top and bottom layers of the 20 ft upward and downward penetration cases, respectively. After 3.5 years of production, no stress reversal occurs in the bottom layer of the 20 ft upward penetration case, as shown in Fig. 13b. In contrast, Fig. 13d shows the 20 ft downward penetration case gives some stress reversal along the prospective infill line in the bottom layer. Moreover, a comparison of Fig. 13a and c indicates that an upward fracture penetration expands the stress reversal to the SRV-projected region in the top layer. However, both cases hold a similar severity of S_{Hmax} reorientation along with the prospective infill location at the top layer.

Figure 14a shows the orientation change of S_{Hmax} along the prospective infill line for the 20 ft upward and downward penetration cases. Although the fracture penetration direction is opposite, the top and middle layers of the two cases experience nearly the same orientation change along the observation line at 3.5 years of parent-well production (i.e., solid/dashed blue lines and solid/dashed red lines). The bottom layer undergoes more obvious S_{Hmax} reorientation with downward penetration than the upward one. For example, the orientation change of S_{Hmax} at the bottom-layer center is almost 90° (i.e., dashed green lines) with a downward penetration. Figure 14b presents the magnitude variation of S_{hmin} under the different scenarios of fracture penetration. Because the fracture penetration is constrained within the extremely tight interlayer, the higher hydraulic fracture does not significantly change the magnitude of S_{hmin} over the production and potential targets. Thus, fracture penetration may not cause a considerable change in the magnitude of S_{hmin} , but could induce a significant difference in the stress reorientation.

The influence of the fracture penetration on the CTSR at the layer center is shown in Fig. 15a. Varying the extent of fracture penetration, i.e., 10 ft and 20 ft, and the direction of fracture penetration, i.e., upwards and downwards, has negligible influence on the CTSR of the top and middle layers. This is understandable since the total fracturing area within the middle layer keeps the same, and the fluid drainage from the top layer is largely gravity-assisted. Meanwhile, either with upward or downward penetration, the CTSR of the bottom layer is shortened as the greater fracturing volume promotes the bottom-layer depletion. However, penetrating downwards does cause a much earlier occurrence of stress reversal in the bottom layer. Figure 15b shows the temporal change of S_{hmin} at the layer center. A tiny increase in S_{hmin} in the top layer and a small decrease in S_{hmin} in the bottom layer are observed as the fracture penetration shifts from upwards to downwards. Owing to the early occurrence of stress reversal or possible fracture hits, parent-well fracture penetration should be carefully considered if an infill well will be drilled and completed in the bottom potential target.

5.3 Effect of Differential Stress

The difference between the maximum and minimum horizontal stresses, i.e., differential stress (DS), is a key parameter determining the speed of stress reorientation and redistribution. In this section, the interlayer geomechanical heterogeneity is introduced by keeping DS of the middle layer and two interlayers as 300 psi and varying that of the top and bottom layers simultaneously from 200 to 400 psi. Other geomechanical parameters, as listed in Table 4, remain the same throughout the entire reservoir. Figure 16 shows the orientation change of S_{Hmax} after 3 years of production when the DS of the top and bottom layers are 250 psi and

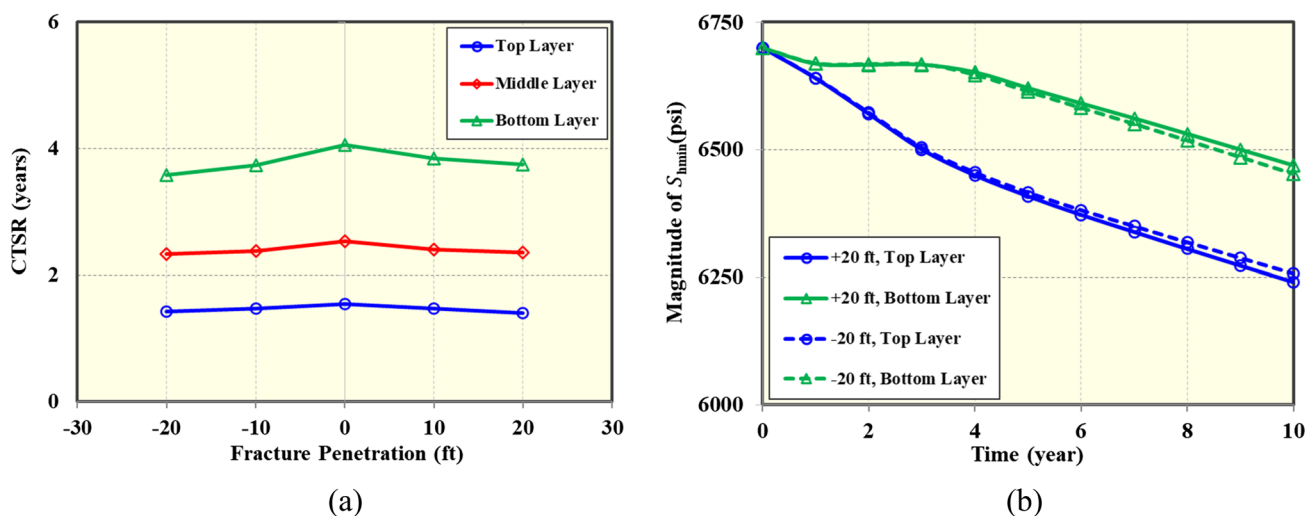


Fig. 15 a Effect of fracture penetration on CTSR and b temporal variation of S_{hmin} . All values are evaluated at the layer center

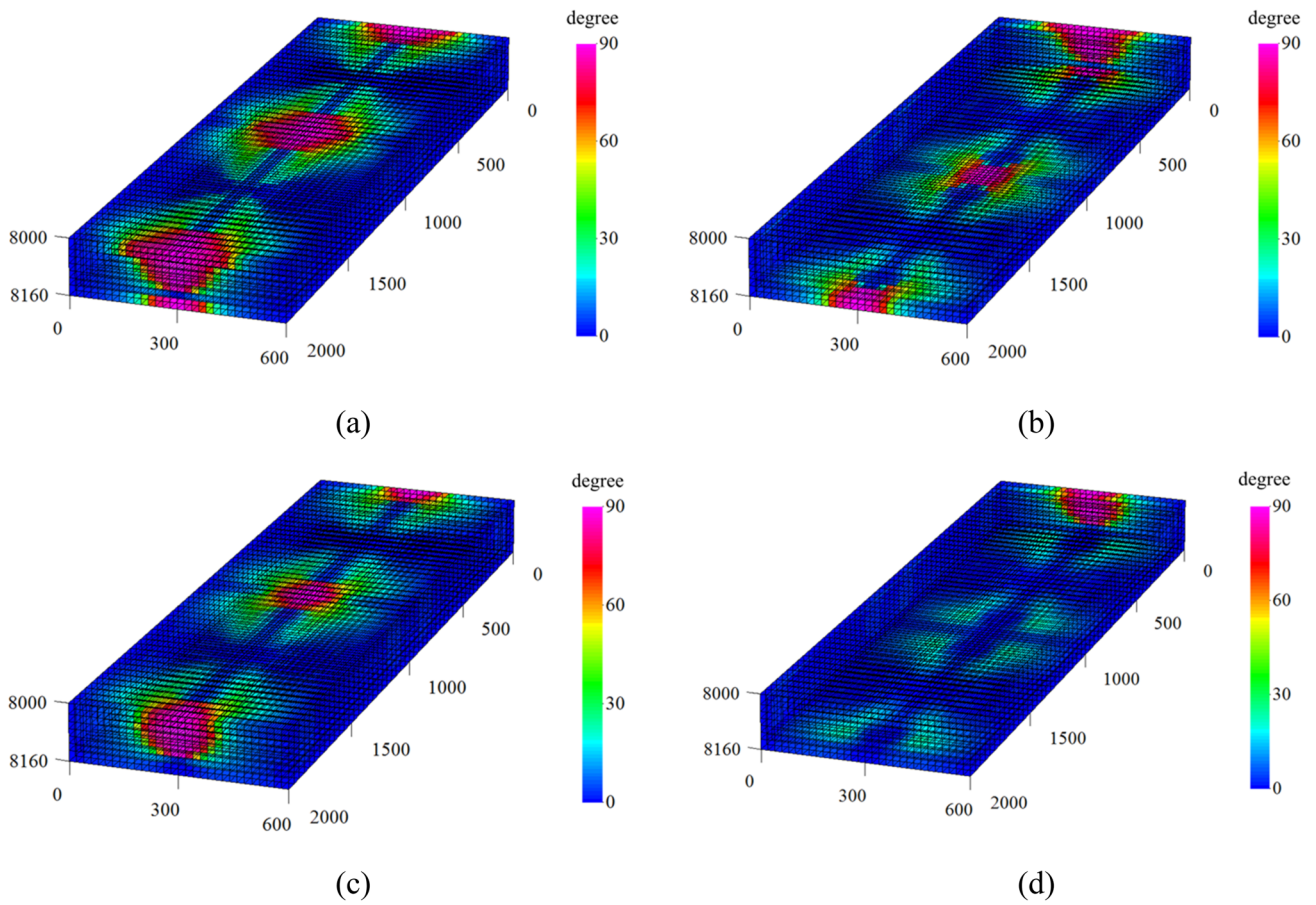


Fig. 16 Orientation change of S_{Hmax} at the top and bottom layers for **a, b** DS=250 psi and **c, d** DS=350 psi after 3 years. Top view: (**a, c**); Bottom view (**b, d**)

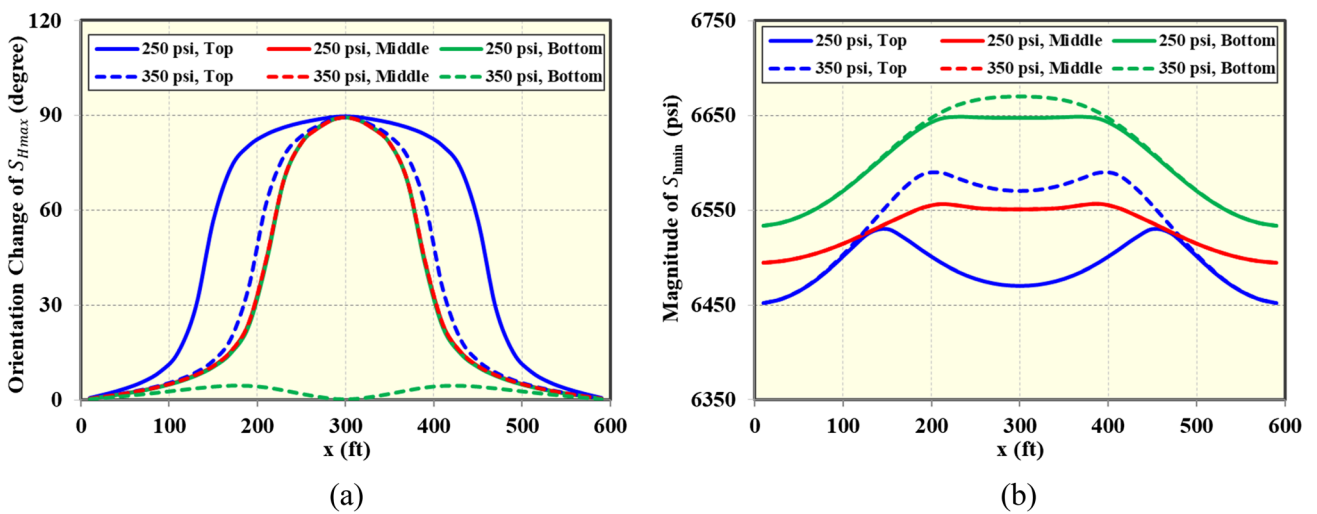


Fig. 17 a Orientation change of S_{Hmax} and **b** magnitude variation of S_{hmin} along prospective infill line at 3 years of parent-well production under different differential stresses

350 psi, respectively. With a smaller DS in the top and bottom layers, a dumbbell-shaped S_{Hmax} reorientation area is observed from the front view in Fig. 16a. Accordingly, as shown in Fig. 16b, stress reversal even occurs along the prospective infill line in the less-depleted bottom layer. If the DS of the top and bottom layers is larger than that of the middle production layer, we observe a rectangle-shaped S_{Hmax} reorientation area over the top and middle layers from the front view of Fig. 16c. However, Fig. 16d indicates that only a small extent of S_{Hmax} reorientation is induced in the bottom layer under higher differential stress. All the findings conclude that differential stress determines not only the spatial distribution of the S_{Hmax} orientation change but also the degree of the S_{Hmax} reorientation.

The orientation change of S_{Hmax} and the magnitude variation of S_{hmin} are plotted along the prospective infill line for the 250 psi and 350 psi cases. At 3 years of parent-well production, as in Fig. 17a, the bottom layer of the 250 psi DS case presents nearly the same extent of S_{Hmax} reorientation as the middle layer does (i.e., solid red and green lines). With a 350 psi DS in the top and bottom layers, the S_{Hmax} reorientation in the top and middle layers are rather similar (i.e., dashed blue and red lines). In contrast, only a minor orientation change of S_{Hmax} occurs in the bottom layer (i.e., dashed green line), which is mainly because the relatively weak drainage in the bottom layer makes it hard to overcome the in-situ horizontal stress contrast. A comparison of the S_{hmin} magnitude indicates that larger differential stress will lead to a higher residual of S_{hmin} around the center of that specific layer, as shown in Fig. 17b. Varying DS of the top and bottom layers from 250 to 350 psi, we observe a 100 psi increase of S_{hmin} at the top-layer center but a negligible 20 psi increase in the bottom layer. Hence, the differential stress

affects the S_{Hmax} orientation change more in the bottom layer and the S_{hmin} magnitude more in the top layer.

Figure 18a shows the CTSR change under various differential stresses for the top, middle, and bottom targets. Since the middle production layer holds a constant fracturing volume and differential stress throughout all tests, there is no change of CTSR at the central point of the middle layer. However, the CTSR of the top layer shows an approximately linear increase as the differential stress gets larger, whereas an exponential increase is observed for the bottom layer. This phenomenon indicates that the interlayer DS heterogeneity has more influence on the CTSR of the bottom layer than that of the top layer. Moreover, higher differential stress results in a much larger S_{hmin} after the stress reversal occurs, as shown in Fig. 18b. Thus, for horizontal infill drilling in the bottom layer, we need to proceed carefully if the differential stress is relatively low in that layer.

5.4 Effect of Rock Stiffness

In this section, we change the rock stiffness, which is represented by Young's modulus (E), of the top and bottom targets between 20 and 40 GPa while keeping other layers constant at 30 GPa. When Young's modulus of the top and bottom layers is 20 GPa, most of the S_{Hmax} reversal is constrained within the middle production layer after 3 years, as shown in Fig. 19a. However, as in Fig. 19b, when Young's modulus of the potential targets increases to 40 GPa, severe orientation changes of S_{Hmax} occur in both the top and bottom layers, and there is nearly no stress reorientation in the middle layer. The reason why production and potential targets respond differently to the variation of Young's modulus can be concluded as two aspects: (1) depleting the stiffer, unstimulated potential targets induces less noticeable

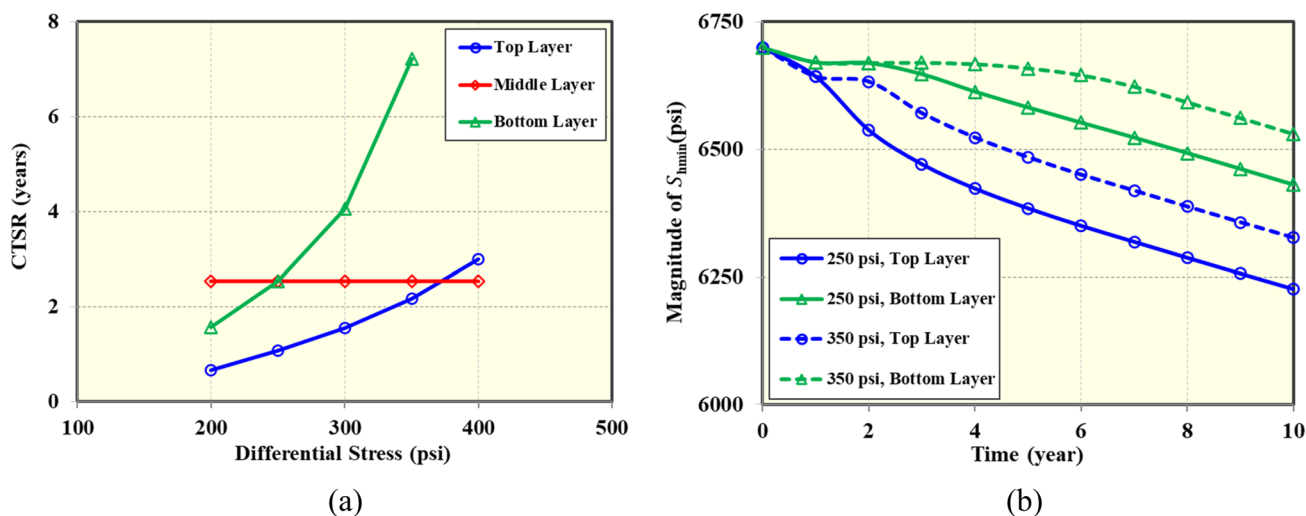


Fig. 18 a Effect of differential stress on CTSR and b temporal variation of S_{hmin} . All values are evaluated at the layer center

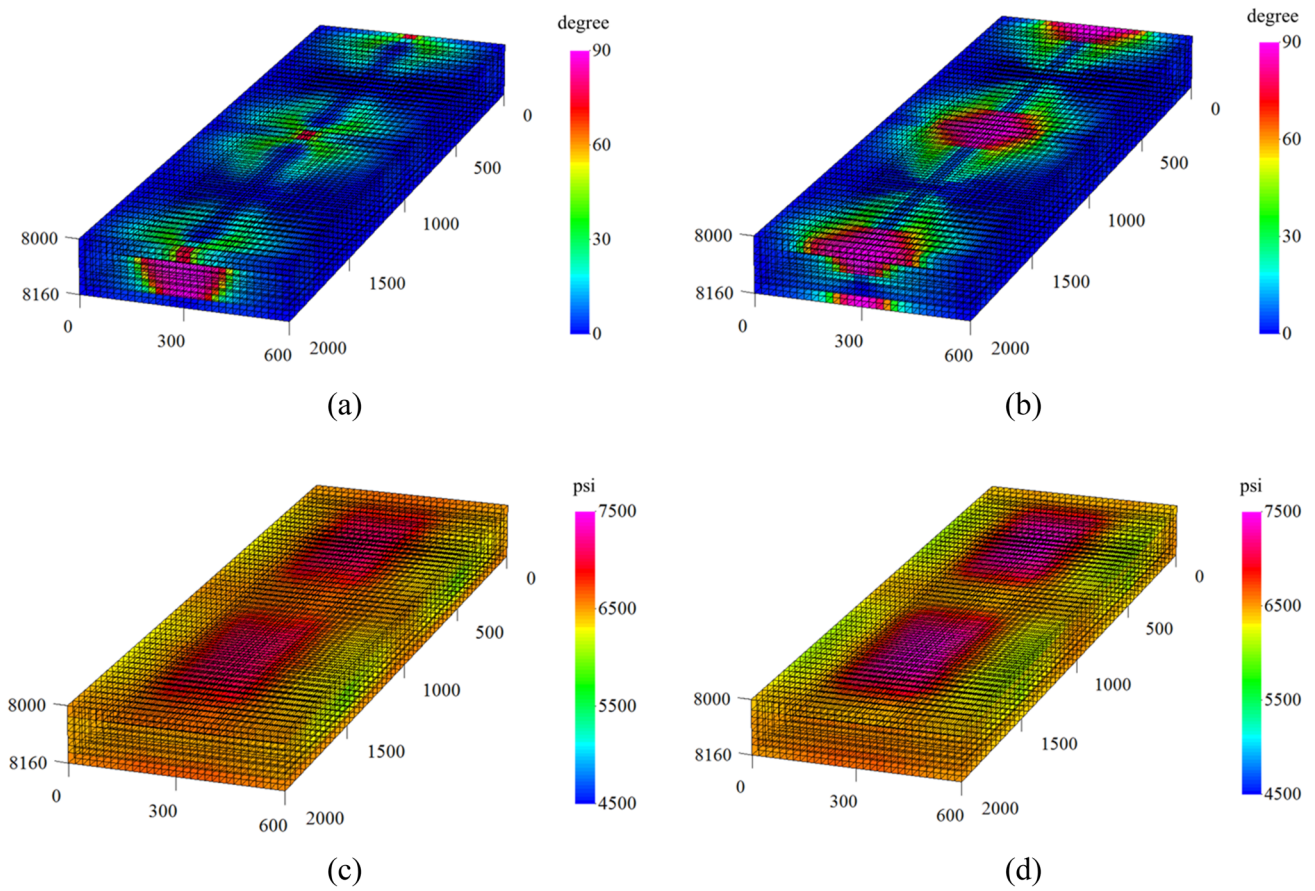


Fig. 19 Comparison between $E=20$ GPa and $E=40$ GPa after 3 years for **a** orientation change of S_{Hmax} at $E=20$ GPa, **b** orientation change of S_{Hmax} at $E=40$ GPa, **c** magnitude distribution of S_{hmin} at $E=20$ GPa, and **d** magnitude distribution of S_{hmin} at $E=40$ GPa

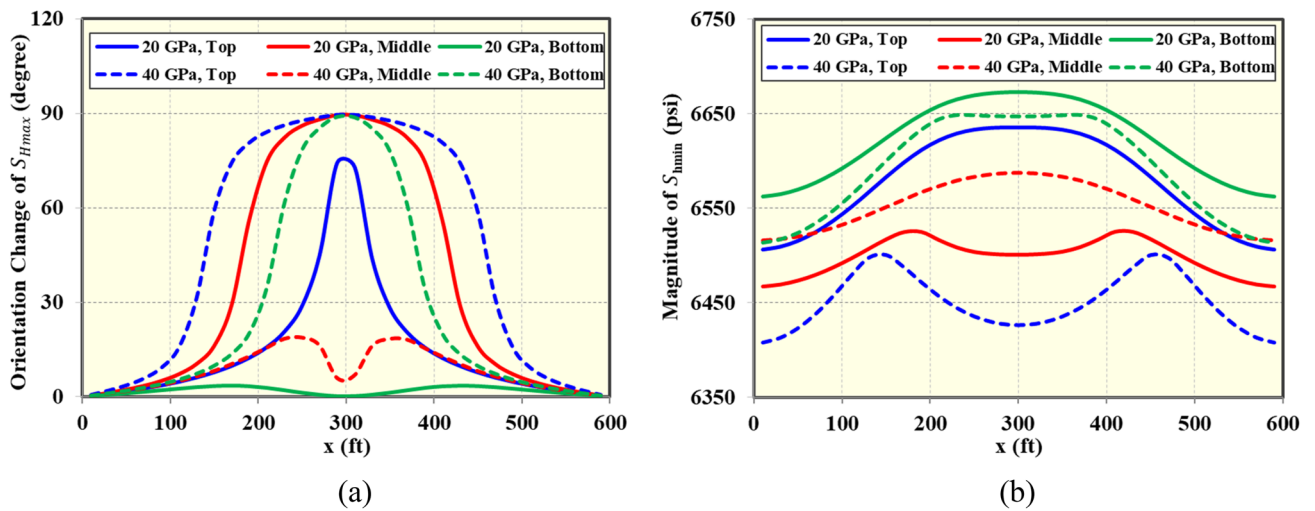


Fig. 20 **a** Orientation change of S_{Hmax} and **b** magnitude variation of S_{hmin} along prospective infill line at 3 years of parent-well production under different rock stiffnesses

compaction compared to the softer rock; thus, the porosity and permeability of a stiffer rock tend to retain, leading to much faster fluid drainage and more severe S_{Hmax} reorientation; (2) for the middle production target, no change in Young's modulus is introduced; however, more fluid from the top and bottom stiffer layers will flow into the middle layer, resulting in slower pressure depletion and smaller stress variation. Figure 19c and d further confirm these illustrations. The higher Young's modulus causes a relatively smaller S_{hmin} magnitude over the entire domain, which verifies the above-mentioned faster pressure drop due to the higher residual permeability of a stiffer formation. A slightly higher S_{hmin} over the SRV-projected region in the 40 GPa case is also observed because of the two-way coupling between fluid flow and solid deformation.

As shown in Fig. 20a, the middle layer in the 20 GPa case shows the most significant S_{Hmax} orientation change at 3 years of parent-well production, followed by the top and bottom layers. However, when Young's modulus of the potential targets increases to 40 GPa, apparent S_{Hmax} reorientation is observed in these layers (dashed blue and green lines) along the prospective infill line. In contrast, the orientation change becomes limited in the middle production layer (dashed red line), which is consistent with the 3D field map analysis. Figure 20b shows the spatial variation of S_{hmin} magnitude in each layer. Under most conditions, a stronger S_{Hmax} reorientation corresponds to a smaller S_{hmin} . However, even the S_{Hmax} orientation change is small in the production target of the 40 GPa case, local principal stresses in the middle layer still decrease much faster than those in the bottom layer due to a much quicker pressure depletion created by hydraulic fractures.

Upon a set of sensitivity analyses, the impact of Young's modulus on the layer-center CTSR is summarized in Fig. 21a for the top, middle, and bottom targets. We observe that the

CTSR of the top and bottom layers are negatively related to Young's modulus, whereas the CTSR of the middle layer shows a positive correlation with the potential layers' stiffness change. As discussed at the beginning of this section, these phenomena are attributed to the multilayer pressure and stress interactions. Although the top and bottom layers share a similar trend regarding the CTSR change, stress reversal tends to occur earlier in the top layer. The magnitude change of S_{hmin} over time is shown in Fig. 21b. Increasing Young's modulus of the potential targets does incur some S_{hmin} drop, i.e., 270 psi at the top-layer center and 160 psi at the bottom-layer center, at the end of the simulation. Owing to more significant stress reorientation and depletion, we should be more cautious about placing a horizontal infill well in a stiffer top target.

6 Conclusions and Suggestions

In this work, we developed a 3D explicitly coupled geomechanics and multiphase compositional model to simulate the stress interference associated with parent-well production in multilayer unconventional reservoirs. The complex fracture geometry under stress shadow effect was incorporated in our coupled model with EDFM, and FEM captured the depletion-induced solid deformation. The impacts of reservoir permeability and fracture penetration on stress responses of the top and bottom targets were investigated under geomechanical homogeneous conditions, and the impacts of differential stress and rock stiffness were studied for geomechanical heterogeneous conditions. We monitored the orientation change of S_{Hmax} and the magnitude variation of S_{hmin} to provide comprehension of the multilayer stress interference. Moreover, rules of thumb were provided to help

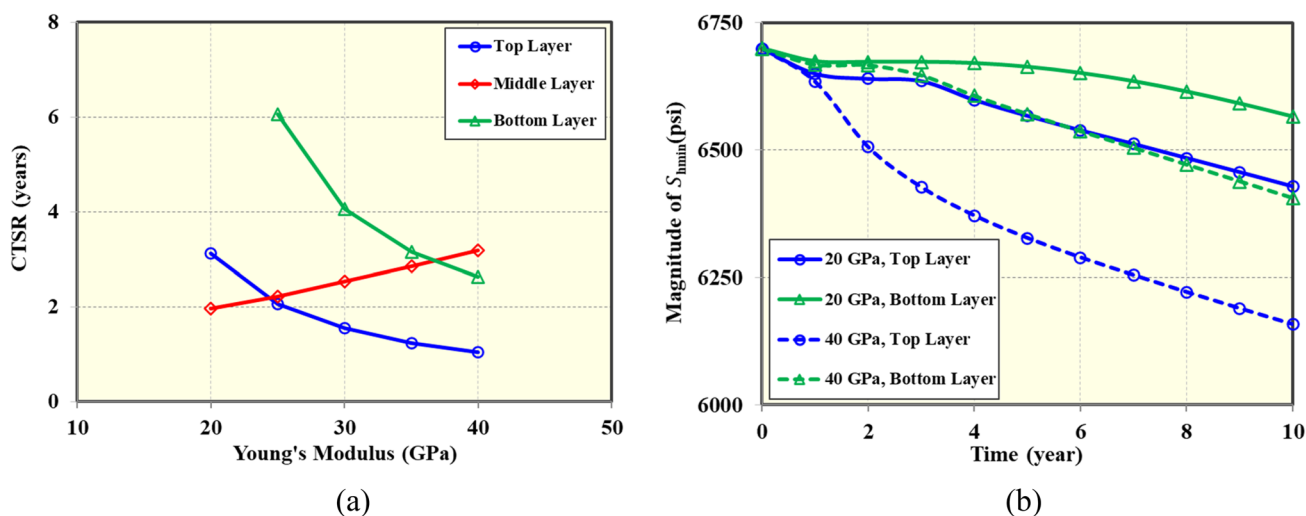


Fig. 21 a Effect of Young's modulus on CTSR and b temporal variation of S_{hmin} . All values are evaluated at the layer center

with the infill operations in adjacent potential layers. The main findings include:

- (a) Stress reorientation induced by parent-well production not only occurs within the production target but also vertically propagates towards adjacent layers, and the extent of stress reversal depends on the relative decline rate of x - and y -direction stresses in each layer;
- (b) The orientation and magnitude change of principal stresses follow a similar trend in all layers under geomechanical homogeneous conditions, whereas the interlayer geomechanical heterogeneity may induce different stress responses between the production and potential targets;
- (c) A higher reservoir permeability results in greater S_{Hmax} reorientation and lower S_{Hmin} along with the prospective infill location. The top layer always shows an earlier occurrence of stress reversal as compared to the middle and bottom layers. Detailed stress modeling is strongly recommended if a horizontal infill well is placed in the top layer of a high-permeability reservoir;
- (d) The extent and direction of fracture penetration have a negligible influence on the orientation and magnitude change of principal stresses in the top and middle layers. However, the bottom-layer CTSR is shortened, no matter with upward or downward penetration. Penetrating downwards will cause an earlier stress reversal in the bottom layer as compared to penetrating upwards;
- (e) As the differential stress of potential targets increases, a linear increase of the CTSR is observed in the top layer and an exponential rise in the bottom layer. Moreover, higher differential stress leads to a larger residual of S_{Hmin} although it keeps nearly unchanged before the CTSR. Horizontal infill drilling in the bottom layer should be conducted with care if the differential stress is relatively low in that layer;
- (f) Varying the rock stiffness (i.e., Young’s modulus) of potential targets causes a negative correlation with the CTSR in these layers and a positive correlation with the CTSR in the middle layer. The impact of Young’s

modulus on the orientation change of S_{Hmax} follows a similar trend in the top and bottom layers, but a more significant S_{Hmin} drop occurs in the top layer.

Appendix A

The McNamee–Gibson problem is solved using Laplace and Fourier transformations (1960a, b). The analytical solutions for excess pore pressure and consolidation settlement are provided as follows.

- Excess pore press (p)

$$p(x, z) = 2G \left(\frac{\partial S}{\partial z} - \eta e \right), \tag{34}$$

where

$$2G \frac{\partial S}{\partial z} = \frac{\eta}{2\eta - 1} \int_0^\infty K(x, \xi) e^{-\xi z} \left[1 + \operatorname{erf}(\xi \sqrt{t}) + \frac{\eta - 1}{\eta} e^{-\frac{2\eta - 1}{\eta^2} \xi^2 t} \operatorname{erfc} \left(\frac{\eta - 1}{\eta} \xi \sqrt{t} \right) \right] d\xi, \tag{35}$$

$$2G\eta e = \frac{\eta}{2\eta - 1} \int_0^\infty K(x, \xi) e^{-\xi z} \left[e^{-\xi z} \operatorname{erfc} \left(\frac{z}{2\sqrt{t}} - \xi \sqrt{t} \right) + \frac{\eta - 1}{\eta} e^{-\frac{2\eta - 1}{\eta^2} \xi^2 t + \frac{\eta - 1}{\eta} \xi z} \operatorname{erfc} \left(\frac{\eta - 1}{\eta} \xi \sqrt{t} + \frac{z}{2\sqrt{t}} \right) \right] d\xi, \tag{36}$$

$$K(x, \xi) = \frac{2}{\pi \xi} \cos(x\xi) \sin \xi, \tag{37}$$

where G is the shear modulus, $G = E/2(1 + \nu)$; η is an auxiliary elastic constant, $\eta = (1 - \nu)/(1 - 2\nu)$; e is the dilation of the soil skeleton, $e = -(\partial u_x/\partial x + \partial u_z/\partial z)$; and u_x, u_z are the horizontal and vertical displacement, respectively.

- Consolidation settlement ($[u_z - u_{z,t=0}]_{z=0}$)

$$[u_z(x) - u_z(x)_{t=0}]_{z=0} = \frac{1}{2G} \frac{\eta}{2\eta - 1} \int_0^\infty \frac{1}{\xi} K(x, \xi) \left\{ \operatorname{erf}(\xi \sqrt{t}) - \frac{\eta - 1}{\eta} \left[1 - e^{-\frac{2\eta - 1}{\eta^2} \xi^2 t} \operatorname{erfc} \left(\frac{\eta - 1}{\eta} \xi \sqrt{t} \right) \right] \right\} d\xi, \tag{38}$$

For special case $\eta = 1$, i.e., the Poisson’s ratio of the medium is equal to zero, the consolidation settlement can be simplified as

$$[u_z(x) - u_z(x)_{t=0}]_{z=0} = \frac{1}{2G} \sqrt{\frac{t}{\pi}} \left[\operatorname{erf} \left(\frac{1+x}{2\sqrt{t}} \right) + \operatorname{erf} \left(\frac{1-x}{2\sqrt{t}} \right) \right] + \frac{1}{2\pi} \left[\begin{aligned} &(1+x) \operatorname{Ei} \left\{ -\frac{(1+x)^2}{4t} \right\} \\ &+ (1-x) \operatorname{Ei} \left\{ -\frac{(1-x)^2}{4t} \right\} \end{aligned} \right], \tag{39}$$

We choose a as the characteristic length and a^2/c as the characteristic time to convert the pressure and displacement formulations into dimensionless form, where c is the coefficient of consolidation defined as $c = 2G\eta k/\mu$.

Acknowledgements This research is supported by the Reservoir Simulation Joint Industry Project (RSJIP) at the Center for Subsurface Energy and the Environment at The University of Texas at Austin. The authors would also like to acknowledge the Texas Advanced Computing Center (TACC) for providing the computational facilities.

Declarations

Conflict of interest The authors declare that they have no conflict of interest.

References

- Ajisafe FO, Solovyeva I, Morales A et al (2017) Impact of well spacing and interference on production performance in unconventional reservoirs, Permian Basin. In: Paper presented at the SPE/AAPG/SEG unconventional resources technology conference, Austin, Texas, USA
- Biot MA (1941) General theory of three-dimensional consolidation. *J Appl Phys* 12:155–164
- Biot MA (1955) Theory of elasticity and consolidation for a porous anisotropic solid. *J Appl Phys* 26(2):182–185
- Cai M (2013) Fracture initiation and propagation in a brazilian disc with a plane interface: a numerical study. *Rock Mech Rock Eng* 46:289–302
- Chang YB (1990) Development and application of an equation of state compositional simulator. In: PhD Dissertation, The University of Texas at Austin, Austin, Texas, USA
- Chin LY, Raghavan R, Thomas LK (2000) Fully-coupled geomechanics and fluid-flow analysis of wells with stress-dependent permeability. *SPE J* 5(1):32–45
- Cipolla C, Motiee M, Kechemir A (2018) Integrating microseismic, geomechanics, hydraulic fracture modeling, and reservoir simulation to characterize parent well depletion and infill well performance in the Bakken. In: Paper presented at SPE/AAPG/SEG unconventional resources technology conference, Houston, Texas, USA
- David C, Wong T, Zhu W, Zhang J (1994) Laboratory measurement of compaction-induced permeability change in porous rocks: implications for the generation and maintenance of pore pressure excess in the crust. *PAGEOPH* 143(1):425–456
- Defeu C, Williams R, Shan D, Martin J, Cannon D, Clifton K, Lollar C (2019) Case study of a landing location optimization within a depleted stacked reservoir in the midland basin. In: Paper presented at the SPE hydraulic fracturing technology conference and exhibition, The Woodlands, Texas, USA
- Ferrill DA, McGinnis RN, Morris AP, Smart KJ, Sickmann ZT, Bentz M, Lehmann D, Evans MA (2014) Control of mechanical stratigraphy on bed-restricted jointing and normal faulting: eagle ford formation, South-Central Texas. *AAPG Bull* 98(11):2477–2506
- Guo X, Wu K, Killough J (2018) Investigation of production-induced stress changes for infill-well stimulation in Eagle Ford shale. *SPE J* 23(4):1372–1388
- Guo X, Wu K, An C, Tang J, Killough J (2019) Numerical investigation of effects of subsequent parent-well injection on interwell fracturing interference using reservoir-geomechanics-fracturing modeling. *SPE J* 24(4):1884–1902
- Gupta J, Zielonka M, Albert RA, El-Rabaa AM, Burnham HA, Choi NH (2012) Integrated methodology for optimizing development of unconventional gas resources. In: Paper presented at the SPE hydraulic fracturing technology conference, The Woodlands, Texas, USA
- Haddad M, Sepehrnoori K (2017) Development and validation of an explicitly coupled geomechanics module for a compositional reservoir simulator. *J Petrol Sci Eng* 149:281–291
- King GE, Rainbolt MF, Swanson C (2017) Frac hit induced production losses: evaluating root causes, damage location, possible prevention methods and success of remedial treatments. In: Paper presented at SPE annual technical conference and exhibition, San Antonio, Texas, USA
- Lake LW (1989) Enhanced oil recovery. Prentice Hall, Englewood Cliffs
- Li N, Wu K, Killough J (2020) Investigation of poor child well performance in the meramec stack play, Anadarko Basin. In: Paper presented at the SPE/AAPG/SEG unconventional resources technology conference, Virtual
- Li L, Lee SH (2008) Efficient field-scale simulation of black oil in a naturally fractured reservoir through discrete fracture networks and homogenized media. *SPE Reser Eval Eng* 11(4):750–758
- Lin M, Chen S, Mbia E, Chen Z (2018) Application of reservoir flow simulation integrated with geomechanics in unconventional tight play. *Rock Mech Rock Eng* 51:315–328
- Lindsay G, Miller G, Xu T, Shan D, Baihly J (2018) Production performance of infill horizontal wells vs. pre-existing wells in the major US unconventional basins. In: Paper presented at SPE hydraulic fracturing technology conference and exhibition, The Woodlands, Texas, USA
- Liu L, Liu Y, Yao J, Huang Z (2020) Efficient coupled multiphase-flow and geomechanics modeling of well performance and stress evolution in shale-gas reservoirs considering dynamic fracture properties. *SPE J* 25(3):1523–1542
- Marongiu-Porcu M, Lee D, Shan D, Morales A (2016) Advanced modeling of interwell-fracturing interference: an Eagle Ford shale-oil study. *SPE J* 21(5):1567–1582
- McNamee J, Gibson RE (1960a) Displacement functions and linear transforms applied to diffusion through porous elastic media. *Q J Mech Appl Math* 13(1):98–111
- McNamee J, Gibson RE (1960b) Plain strain and axially symmetric problems of the consolidation of a semi-infinite clay stratum. *Q J Mech Appl Math* 13(2):210–227
- Mehra R, Hadjitofi M, Donnelly JK (1982) An automatic time-step selector for reservoir models. In: Paper presented at the SPE reservoir simulation symposium, New Orleans, Louisiana
- Mehrabi M, Pei Y, Haddad M, Javadpour F, Sepehrnoori K (2021) Quasi-static fracture height growth in laminated reservoirs: impacts of stress and toughness barriers, horizontal well landing depth, and fracturing fluid density. In: Paper presented at the SPE/AAPG/SEG unconventional resources technology conference, Houston, Texas, USA
- Miller G, Lindsay G, Baihly J, Xu T (2016) Parent well refracturing: economic safety nets in an uneconomic market. In: Paper presented at SPE low perm symposium, Denver, Colorado, USA
- Moinfar A, Varavei A, Sepehrnoori K, Johns RT (2013) Development of a coupled dual continuum and discrete fracture model for the simulation of unconventional reservoirs. In: Paper presented at the SPE reservoir simulation symposium, The Woodlands, Texas
- Moinfar A, Varavei A, Sepehrnoori K, Johns RT (2014) Development of an efficient embedded discrete fracture model for 3D compositional reservoir simulation in fractured reservoirs. *SPE J* 19(2):289–303
- Pan F (2009) Development and application of a coupled geomechanics model for a parallel compositional reservoir simulator. In: PhD

- dissertation, The University of Texas at Austin, Austin, Texas, USA
- Pei Y, Yu W, Sepehrnoori K (2020) Determination of infill drilling time window based on depletion-induced stress evolution of shale reservoirs with complex natural fractures. In: Paper presented at the SPE improved oil recovery conference, Virtual
- Pei Y, Yu W, Sepehrnoori K, Gong Y, Xie H, Wu K (2021) The influence of development target depletion on stress evolution and infill drilling of upside target in the Permian Basin. *SPE Reserv Eval Eng* 24(3):570–589
- Peng DY, Robinson DB (1976) A new two-constant equation of state. *Ind Eng Chem Fundam* 15(1):59–64
- Raghavan R, Chin LY (2002) Productivity changes in reservoirs with stress-dependent permeability. In: Paper presented at the SPE annual technical conference and exhibition, San Antonio, Texas
- Roussel NP, Florez HA, Rodriguez AA (2013) Hydraulic fracture propagation from infill horizontal wells. In: Paper presented at SPE annual technical conference and exhibition, New Orleans, Louisiana, USA
- Safari R, Lewis R, Ma X, Mutlu U, Ghassemi A (2017) Infill-well fracturing optimization in tightly spaced horizontal wells. *SPE J* 22(2):582–595
- Sangnimmuan A, Li J, Wu K (2018) Development of efficiently coupled fluid flow/geomechanics model to predict stress evolution in unconventional reservoirs with complex-fracture geometry. *SPE J* 23(3):640–660
- Sangnimmuan A, Li J, Wu K, Holditch S (2019) Impact of parent well depletion on stress changes and infill well completion in multiple layers in Permian Basin. In: Paper presented at SPE/AAPG/SEG unconventional resources technology conference, Denver, Colorado, USA
- Sepehrnoori K, Xu Y, Yu W (2020) Embedded discrete fracture modeling and application in reservoir simulation. Amsterdam, The Netherlands: Developments in Petroleum Science, Elsevier
- Suppachoknirun T, Tutuncu AN (2017) Hydraulic fracturing and production optimization in Eagle Ford Shale using coupled geomechanics and fluid flow model. *Rock Mech Rock Eng* 50:3361–3378
- Tang J, Wu K, Zeng B, Huang H, Hu X, Guo X, Zuo L (2018) Investigate effects of weak bedding interfaces on fracture geometry in unconventional reservoirs. *J Petrol Sci Eng* 165:992–1009
- Thiercelin MJ, Plumb RA (1994) A core-based prediction of lithologic stress contrasts in East Texas formations. *SPE Form Eval* 9(4):251–258
- Verruijt A (1995) Computational geomechanics. Kluwer Academic Publishers, Boston
- Wang H, Sharma MM (2019) Determine in-situ stress and characterize complex fractures in naturally fractured reservoirs from diagnostic fracture injection tests. *Rock Mech Rock Eng* 52:5025–5045
- Wang J, Olson JE (2021) Efficient modeling of proppant transport during three-dimensional hydraulic fracture propagation. In: Paper presented at the SPE annual technical conference and exhibition, Dubai, UAE
- Wang J, Lee HP, Li T, Olson JE (2020) Three-dimensional analysis of hydraulic fracture effective contact area in layered formations with natural fracture network. In: Paper presented at the 54th US rock mechanics/geomechanics symposium, Virtual
- Weng X, Siebrits E (2007) Effect of production-induced stress field on refracture propagation and pressure response. In: Paper presented at the SPE hydraulic fracturing technology conference, College Station, Texas, USA
- Wu K, Olson JE (2015) Simultaneous multifracture treatments: fully coupled fluid flow and fracture mechanics for horizontal wells. *SPE J* 20(2):337–346
- Xu Y, Cavalcante Filho JSA, Yu W, Sepehrnoori K (2017) Discrete-fracture modeling of complex hydraulic-fracture geometries in reservoir simulators. *SPE Reserv Eval Eng* 20(2):403–422
- Yue K, Olson JE, Schultz RA (2019) The effect of layered modulus on hydraulic-fracture modeling and fracture-height containment. *SPE Drill Complet* 34(4):356–371
- Zhang J, Standifird W, Roegiers JC, Zhang Y (2007) Stress-dependent fluid flow and permeability in fractured media: from lab experiments to engineering applications. *Rock Mech Rock Eng* 40:3–21

Publisher's Note Springer Nature remains neutral with regard to jurisdictional claims in published maps and institutional affiliations.